Marine Geology Volume 430, December 2020, 106337
https://doi.org/10.1016/j.margeo.2020.106337

Manuscript submitted to Marine Geology:

A single-stage megaflood at the termination of the Messinian salinity crisis: Geophysical and modelling evidence from the eastern Mediterranean Basin

Daniele Spatola[1], José David del Moral-Erencia[2], Aaron Micallef[1,3*], Angelo Camerlenghi[4], Daniel Garcia-Castellanos[5], Sanjeev Gupta[6], Patricio Bohorquez[2], Marc-André Gutscher[7], Claudia Bertoni[8]

1 Marine Geology & Seafloor Surveying, Department of Geosciences, University of Malta, Msida, Malta
2 Centro de Estudios Avanzados en Ciencias de la Tierra (CEACTierra), Universidad de Jaén, Jaén, Spain
3 Helmholtz Centre for Ocean Research, GEOMAR, Kiel, Germany
4 Istituto Nazionale di Oceanografia e di Geofisica Sperimentale (OGS), Trieste, Italy
5 Instituto de Ciencias de la Tierra Jaume Almera, ICTJA-CSIC, Barcelona, Spain
6 Department of Earth Science and Engineering, Imperial College London, London, UK
7 Laboratoire Géosciences Océan, University of Brest/CNRS, IUEM, Pl. N. Copernic, Plouzané, 29280, France
8 Department of Earth Sciences, University of Oxford, Oxford, UK

*Corresponding author:
E-mail: aaron.micallef@um.edu.mt; Telephone: +356 23403662; Address: 37, Triq ta' Xmiexi, Msida, Malta

ABSTRACT

The Messinian salinity crisis was an extraordinary event that resulted in the deposition of kilometre-thick evaporite sequences in the Mediterranean Sea after the latter became disconnected from the world's oceans. The return to fully and stable marine conditions at the end of the crisis is still subject to debate. Three main hypotheses, based on geophysical and borehole data, onshore outcrops and climate simulations, have been put forward. These include a single-stage catastrophic flood, a two-step reflooding scenario, and an overspill of Paratethyan water followed by Atlantic inflow. In this study, two research questions are addressed: (i) Which event marked the termination of the Messinian salinity crisis?; (ii) What was the sea level in the eastern Mediterranean Sea during this event? Geophysical data from the western Ionian Basin are integrated with numerical simulations to infer that the termination of the crisis consisted of a single-stage megaflood following a sea level drawdown of 1900 m. This megaflood deposited an extensive sedimentary body with a chaotic to transparent seismic signature at the base of the Malta Escarpment. Fine, well-sorted sediments are predicted to have been deposited within the thicker sections of the flood deposit, whereas a more variable distribution of coarser sediments is expected elsewhere. The north-western Ionian Basin hosts evidence of episodic post-Messinian salinity crisis slope instability events in the last ~1.8 Ma. The largest of these emplaced a >200 km^3 deposit and is associated with failure of the head of Noto Canyon (offshore SE Sicily). Apart from unravelling the final phase of the Messinian salinity crisis and the ensuing stratigraphic evolution of the western Ionian Basin, our results are also relevant to better understand megafloods, which are some of the most catastrophic geological processes on Earth and Mars.

Keywords: Zanclean flood; megaflood; geophysics; numerical modelling; Messinian salinity crisis; Mediterranean Sea

1. INTRODUCTION

The Messinian salinity crisis (MSC) was an extraordinary, short-term (~ 640 ka), geological, oceanographic and ecological event that occurred between 5.97 and 5.33 Ma and that had local to global consequences (Gennari et al., 2013; Meilijson et al., 2019; Rouchy and Caruso, 2006; Roveri et al., 2014; Ryan, 2009). During this time, the Mediterranean Sea became disconnected from the world's oceans (Weijermars, 1988), and excess evaporation with respect to river run-off and precipitation led to the deposition of salt that reached a thickess of >3 km locally (Lofi et al., 2011a, b, 2018). The total volume of salt had previously been estimated at >2 million km^3, equivalent to 6-10% of the total dissolved oceanic salt (Blanc, 2000; Flecker et al., 2015; Ryan, 2009). However, a recent study, based on a dense compilation of seismic prospection surveys, revised this estimate to 821–927 thousand km^3 (Haq et al., 2020), which is equivalent to ~4% of the world's present oceanic salt in dissolution.

The concept of the MSC was first proposed by Selli (1954), who correlated the gypsum deposits outcropping in the northern Apennine chain to a widespread and dramatic increase in seawater salinity in the entire Mediterranean region at the end of the Miocene. Scientific drilling in the central Messina Abyssal Plain in the Ionian Basin (Deep Sea Drilling Project (DSDP) Site 374; Figure 1) retrieved evaporites from the uppermost part of the Messinian sequence, providing evidence for the theory of the Messinian desiccation of the Mediterranean Sea (Hsü et al., 1978). Since then, multiple and contrasting hypotheses have been proposed for the origin of the Messinian evaporite deposits. According to the shallow-water, deep-basin model, sea level drawdown by a maximum of 1000-4000 m from present-day level transformed the Mediterranean Basin into a complex of hypersaline lakes in which deposition of kilometre-thick sequences of salts occurred (Barber, 1981; Ben-Gai et al., 2005; Bertoni and Cartwright, 2005; Druckman et al., 1995; Gargani and Rigollet, 2007; Lofi, 2002; Madof et al., 2019; Maillard and Mauffret, 1993; Micallef et al., 2019; Pellen et al., 2019; Ryan, 1976; Stampfli and Höcker, 1989; Steckler et al., 2003; Tibor and Ben-Avraham, 2005; Urgeles et al., 2011). Drawdown estimates were derived from analysis of seismic reflection data from the rim of the Mediterranean that contained the evaporite pinch-out and MSC erosional landforms. Recently, however, some studies have proposed that the evaporitic deposition occurred without a substantial sea level drawdown, giving rise to an alternative scenario represented by a deep-water, deep-basin depositional model (Roveri et al., 2001; Lugli et al., 2015, among others). Following the Messinian phase of salt deposition under hypersaline conditions, there was a transition to a phase of sediment deposition in a freshwater environment, which is represented by the so-called "Lago-Mare" sedimentary facies. These facies contain microfossils originating from the eastern part of the Mediterranean Sea, from the so-called Neogene 'Paratethys basin' (Carpathian and Black Sea areas) (e.g. Krijgsman et al., 2010). This phase of sediment deposition led to the end of the MSC.

The return to fully and stable marine conditions at the end of the MSC was geologically instantaneous, as indicated by a sharp lithological and paleontological boundary in sediment cores (Van Couvering et al., 1971). One scenario proposed for the termination of the MSC involves refilling the Mediterranean Basin through the present Strait of Gibraltar with a large volume of Atlantic waters in a megaflood event, the so-called Zanclean flood (Blanc, 2002; Garcia-Castellanos et al., 2020, 2009). Studies based on borehole and seismic reflection data reported evidence for a ~390 km long, 200-600 m deep and 2-8 km wide erosional channel incised into bedrock between the Gulf of Cadiz and the Alborán Sea, across the Camarinal Sill in the Strait of Gibraltar (Esteras et al., 2000; Palomino et al., 2009). Garcia-Castellanos et al. (2009) postulated that the deep channel was excavated by the Zanclean flood. By coupling a hydrodynamic calculation of water discharge and the erosion implied by the water flow, they estimated that 90% of the water was transferred from the Atlantic Ocean into the Mediterranean Sea in a short period of time, ranging from few months to two years. This estimation is subject to the assumption that the entire depth of the erosive channel in the Camarinal Sill is related to the flood event (Abril and Periáñez, 2016). More recently, evidence for the deposition of the material eroded by the postulated Zanclean flood in the Strait of Gibraltar has been identified. This includes a series of elongated sedimentary bodies at the base of the Pliocene in the Alborán Sea that are 35 km long, 160 m thick and up to 7 km wide. These are located parallel and next to the erosion channel, and have been tentatively interpreted as megabar deposits resulting from the flood (Estrada et al., 2011; Periáñez et al., 2019). At the base of the Malta Escarpment in the central Mediterranean Sea (Figure 1), Micallef et al. (2018) reported evidence for an extensive chaotic deposit overlying the Messinian evaporite succession, which they interpreted as generated by the Zanclean flood during the overspill of floodwaters from the western to the eastern Mediterranean Basin. SE Sicily has been proposed as the gateway for the Zanclean flood. This inference is primarily based on the occurrence of the Noto Canyon, a large box canyon carved into the Malta Escarpment, and a buried 4 km wide and 400 m deep channel located on the shelf upslope of the canyon (Micallef et al., 2018).

Alternative hypotheses exist for the termination of the MSC. Offshore seismic evidence of bedrock terraces cut by erosion, such as wave ravinement processes, and onshore outcrops have been used to propose a two-step reflooding scenario, with a slow and moderate first stage followed by a rapid and dramatic second stage (Bache et al., 2012, 2009). The occurrence of brackish lacustrine Lago-Mare deposits stratigraphically overlying the Messinian salts, on the other hand, has been used to question the megaflood hypothesis. Instead, these deposits may suggest that an initial overspill of Paratethyan water, derived from the former Black Sea, entered the Mediterranean Basin and was followed by Atlantic inflow once the Mediterranean Basin was refilled (Marzocchi et al., 2016). Sub-precessional climate simulations show a positive freshwater budget for the Paratethys and a negative freshwater budget for the Mediterranean Sea, which would have triggered a 'Mediterranean outflow pump'. This provides an alternative mechanism for the Lago-Mare facies and the end of the MSC (Marzocchi et al., 2016).

The goal of this contribution is to reassess the termination of the MSC through analysis of the seismic stratigraphy of the post-Messinian sedimentary succession preserved in the western Ionian Basin. We address two specific research questions: (i) which event marked the termination of the MSC?; and (ii) what was the sea level in the eastern Mediterranean Sea during this event? We tackle these questions by first analysing 2D seismic reflection profiles from the western Ionian Basin to reconstruct its stratigraphic evolution and identify evidence for megaflood deposition. We then carry out numerical simulations to estimate the behaviour and dynamics of the Zanclean flood and relate these to observations from the seismic reflection profiles.

2. REGIONAL SETTING

2.1. Western Ionian Basin

Located in the eastern Mediterranean Basin, the >3 km deep Ionian Basin is bordered to the west by the Malta Escarpment and eastern Sicilian Margin, to the north by the Calabrian-Peloritan continental block, to the east by the Hellenic Arc, and to the south by the east-west trending Medina Ridge (Figure 1). Although the nature of the underlying crust is still debated, most researchers agree that the western Ionian Basin is a remnant of the Mesozoic Tethys Ocean crust, of Triassic or pre-Triassic age, which transitions into continental crust along the western and southern margins (Carminati et al., 2004; Dannowski et al., 2019; Gallais et al., 2013; Maesano et al., 2017; Polonia et al., 2016; San Pedro et al., 2017; Speranza et al., 2012). The Ionian lithosphere is undergoing NW-oriented subduction below the Calabrian Ridge, driven by NW-directed African and Eurasian relative plate convergence (Del Ben et al., 2010; Mantovani et al., 2007). The transition to the Sicilian continental lithosphere to the west is thought to be located at the foot of the Malta Escarpment. A sub-vertical lithospheric tear fault or STEP (sensu Govers & Wortel, 2005) has been proposed by many authors as a lithospheric structure that is nearly parallel to the Malta Escarpment, above which a main right lateral transtensional system cuts into the Calabrian-Peloritan block (Dellong et al., 2018; Gallais et al., 2013; Gutscher et al., 2017; Maesano et al., 2017). The western Ionian Basin also hosts the Alfeo Seamount, a morphologic high known to contain shallow platform carbonate rocks (Argnani and Bonazzi, 2005). The lithosphere is overlain by 5-7 km of sediments ranging between Jurassic to Recent in age (Cernobori et al., 1996; Speranza et al., 2012). From the Tortonian, the western Ionian Basin has been characterised by abundant accumulation of Messinian evaporites as well as Plio-Pleistocene hemipelagic sediments (Camerlenghi et al., 2019; Gallais et al., 2013; Gutscher et al., 2017).

2.2. The Malta Escarpment

The Malta Escarpment is a steep, 290 km long submarine limestone and dolomite cliff with a relief of >3 km that extends from the eastern margin of Sicily southwards to the Medina Seamounts (Micallef et al., 2019). It marks the transition between the Pelagian Platform in the west (Finetti, 1982) to the Ionian Basin in the east (Figure 1). Outcropping along the Malta

Escarpment are Triassic to Cretaceous shallow platform carbonates and Cretaceous to Miocene shelf edge carbonate deposits (Scandone, 1981), which are overlain by Tortonian to Recent terrestrial, pelagic and hemipelagic strata (Biju-Duval et al., 2006; Jongsma et al., 1985; Max et al., 1993; Micallef et al., 2016, 2011; Osler and Algan, 1999). The processes responsible for the formation of the Malta Escarpment include rifting in the upper-Permian-Triassic, followed by spreading from the Jurassic till the upper Cretaceous-early Tertiary (Ben-Avraham & Grasso, 1991; Catalano et al., 2000a). Catalano et al. (2000b), however, suggested that continental rifting took place from the pre-Triassic till the early Cretaceous. Since the onset of plate convergence between Africa and Europe during the late Cretaceous, the Malta Escarpment was transformed from a passive margin into a mega-hinge fault system with an additional sinistral strike-slip component (Adam et al., 2000). At the fine spatial scale, the Malta Escarpment is characterised by more than two hundred submarine canyons, which were predominantly eroded by sub-aerial processes during the MSC (Micallef et al., 2019). The largest of these canyons are Noto, Cumecs and Heron canyons, which range between 27 and 100 km in length. The Malta Escarpment is also characterised by widespread, small-scale slope failures of Plio-Pleistocene sediments, as well as palaeoshorelines and shore platforms that are indicative of an evaporative drawdown of 1800–2000 m in the eastern Mediterranean Basin (Micallef et al., 2019).

3. MATERIALS AND METHODS

3.1. Geophysical data

Our study is based on the following geophysical data sets collected from the Malta Escarpment and the western Ionian Basin between 1969 and 2015 (Figure 1):

(i) Multibeam echosounder bathymetry data: Multibeam echosounder data sets acquired during three oceanographic cruises - (i) R/V Suroît, CIRCEE-HR, 2013 (Kongsberg Simrad EM302); (ii) R/V OGS Explora, CUMECS-2, 2014: (Reson SeaBat 7150 and 8111); (iii) R/V OGS Explora, CUMECS-3, 2015 (Reson SeaBat 7150 and 8111) – were used to derive bathymetry grids with bin sizes of 15 - 50 m after sound velocity corrections and basic editing (Micallef et al., 2019). These data sets were integrated with published bathymetric data from Gutscher et al. (2017) (60 m grid resolution) and EMODnet bathymetry (http://www.emodnet-bathymetry.eu) (220 m grid resolution). The final bathymetric map combining all multibeam echosounder data covers an area of ~20,000 km^2, extends from the strait of Messina to the Medina Seamounts, and covers a depth range of 100-4000 m.

(ii) Multichannel seismic reflection profiles: 2-D multichannel seismic reflection profiles acquired during the following oceanographic cruises (acquisition methodologies and processing workflows are provided in the cited papers) were used: (i) MS, 1969–1973 (Finetti & Morelli, 1973); (ii) CROP, 1988–1995 (Finetti et al., 2005); (iii) CA-99, 1999: SPECTRUM (now TGS) (Micallef et al., 2018; 2019); (iv) MEM-07, 2007: SPECTRUM (now TGS) (Micallef et al., 2018; 2019); (v) CIRCEE-HR, 2013 (Gutscher et al., 2016); (vi) CUMECS-3, 2015 (Micallef et al., 2018; 2019). Interval velocities were determined using pre-stack depth migration conducted on profile CROP-21; the method used is described in Micallef et al. (2018).

The seismic stratigraphy of the western Ionian Basin was constrained by adopting the seismic stratigraphy described in Camerlenghi et al. (2019) and Lofi et al. (2011a). The interpretation of units from the seismic reflection profiles is based on seismic facies classification. The reflectors marking the top and bottom of each seismic unit were interpreted and extracted as horizons in time. Conversion of these horizons to depth was carried out using the interval velocities in Micallef et al. (2018). The horizons were interpolated into surfaces using a natural neighbour technique. The boundaries of the surfaces were restricted to the area of unit 2. Isopach maps for each unit were generated by subtracting the bottom surface from the top surface.

The age and seismic character of the Messinian evaporitic units are tied to the well-known Messinian seismic markers of the Mediterranean Basin (Lofi et al., 2018). The stratigraphy, age model and sedimentation rates in the Plio-Quaternary section were extrapolated from DSDP Site 374 (Shipboard Scientific Party, 1978) (position in Figure 1), which hosts a post-Messinian sedimentary succession dominated by increasing terrigenous input, inferred to be comparable (from seismic facies and overall thickness) with the sedimentary succession at the base of the Malta Escarpment. ODP Site 964 (Shipboard Scientific Party, 1996) (position Figure 1) was not used because it hosts a thin, condensed hemipelagic succession on the outer part of the Calabrian accretionary complex, which is not considered as representative of our study area. The age of post-Messinian units has been estimated as described in Figures 2a-b by extrapolating the curve of the sedimentation rate obtained at DSDP Site 374 to a representative continuous and expanded section of our survey area, which was converted to depth using the interval velocity described in Micallef et al. (2018). The resulting age model contains approximations due to the use of an average interval velocity for the post-Messinian section, rather than a velocity function, and a poorly constrained sedimentation rate curve at DSDP Site 374 resulting from a poor core recovery. Nevertheless, in the absence of additional borehole information, the proposed age model is the best approximation to a trend of increasing sedimentary input to the basin from the Pliocene to the Pleistocene, which is also confirmed by the well-constrained sedimentation rate curve in the hemipelagic section drilled at ODP Site 964.

3.2. Numerical modelling

A 2-D hydraulic modelling approach was used to estimate the behaviour and dynamics of the Zanclean flood. This 2-D model is based on the Saint-Venant depth-averaged shallow-water equations and has been used to characterise the dynamics of terrestrial megafloods in the Late Pleistocene (Baker, 2020; Bohorquez et al., 2019) and the marine Zanclean megaflood (Abril and Periáñez, 2016; Periáñez et al., 2019). Here, a sophisticated approach, which estimates the original flow field and indicates where flood deposits may be found, was developed. For the first time, the pre-flood bathymetry was accurately reconstructed before the implementation of the hydraulic model so as to simulate the infilling of the eastern Mediterranean Basin without the deposited sediments. To capture the topographic details, the spatial resolution of the computational grid was increased by a factor of 10 in comparison to previously published simulations, leading to high computational costs. Hence, a 2-D model, accelerated by a graphics processing unit that achieves speed-ups of up to two orders of magnitude with respect to CPU models, was used (García-Feal et al., 2018).

The first step of the modelling workflow entailed the reconstruction of the MSC topography using back-stripping. The thickness of the sedimentary units above the evaporites, identified in Micallef et al. (2018), was subtracted from the present bathymetry of the western Ionian Basin. The resulting surface was isostatically restored as explained in Micallef et al. (2019). High-magnitude palaeohydraulic techniques were then used for the calibration of the most-probable hydraulic conditions during the discharge associated with the Zanclean flood (Carrivick, 2006).

The computational domain was defined by a structural mesh with an area of 12,800 km^2 that encompassed the megaflood deposit (Figure 3). A spatial resolution of 50 m was used at Noto Canyon (Figure 1), whereas a 100 m was used for the rest of the computational domain. The unstructured mesh has 1.1 million cells. A subsidence value of 500 m since the MSC was considered, which corresponds to the average value of the range predicted in Micallef et al. (2019). We verified that the inclusion of the eastward variation of subsidence estimated in the previous work would exert a minimal effect on the velocity and flow pattern, particularly above the flood sediment records.

To find the optimal values of the discharge and the initial water level in the western Ionian Basin that led to the formation of unit 2 (section 4.1.2), we performed 290 numerical simulations varying both parameters systematically. Although each simulation was transient, we analysed the steady-state achieved at a later stage (less than 10 days). We set a steady discharge in the inflow, but its value was varied across simulations between 2 and 140 Sv to evaluate the effect of the different water flows. Such bounds were estimated from the modelled Zanclean flood hydrogram in Garcia-Castellanos et al. (2009). The flow magnitude used as input for each simulation implied a nearly constant water level in the western boundary that was computed using the incoming Riemann invariant because of the subcritical flow regime (García-Feal et al., 2018). In the remaining boundaries, the water level was the same as the initial stage, where the flow regime was subcritical, but changed in supercritical areas according to the characteristic variable extrapolation method (Blayo and Debreu, 2005). As an initial condition, we considered a subaerial shelf upstream of the Noto Canyon, while the initial water level at rest further downstream was constant before the Zanclean flood (Figure 3). We varied such a level, systematically, from -2400 to -1500 m below the present sea level in steps of 100 m.

Finally, the hydraulics of a putative, lower-magnitude second flood event that might develop unit 1b (section 4.1.2) was also analysed by running 48 additional simulations. In this case, the same subsidence value of 500 m was used (Micallef et al., 2019). Different pre-second flood sea levels, ranging between -1200 and -500 m below present sea level with a 100 m step size, were used. These values are higher than those set for the first event because the western Ionian Basin was assumed to have been partly infilled. In these numerical simulations, different discharge values ranging between 0.5 and 30 Sv were input. The same mesh as for the previous simulation was used.

4. RESULTS

4.1. Seismic stratigraphy

Six seismic units and sub-units were distinguished on the basis of seismic facies, geometry and character of prominent reflectors (see Figure 2c for the complete stratigraphic scheme).

4.1.1. Unit 3

The stratigraphically lowest unit 3 corresponds to the Messinian evaporite sequence (Figures 2c, 4). It comprises two sub-units: (i) a lower, seismically transparent unit (unit 3b – Mobile Unit (halite) with a marked discordance between the lower, nearly flat boundary (horizon F) and the upper folded boundary (horizon E); the latter is not a clear reflector; and (ii) an upper unit (unit 3a – Upper Unit (gypsum, anhydrite, marls and dolomite; Shipboard Scientific Party, 1978)) consisting of high amplitude reflectors with poor to good lateral continuity, at times chaotic internal configuration, and evidence of irregular folding. The top of unit 3a consists of a continuous and irregular high amplitude seismic reflector, with the same polarity as the seafloor, which is strongly truncated by the overlying unit 2 (horizon D). This truncation surface constitutes a major unconformity. The palaeo-topography of the top of unit 3a is dominated by a depression that is located adjacent, and parallel, to the base of the Malta Escarpment (Figures 5a-b). This depression is ~100 km long, up to 25 km wide and 500 m deep, and oriented NNW-SSE. The palaeo-topography of the top of unit 3a also includes a large positive-relief structure located NE of Noto Canyon and NW of Alfeo Seamount; it is 600 m high, oriented NW-SE, and covers an area of 700 km^2 (Figure 5c).

4.1.2. Unit 2

Unit 2 is a highly distinctive sedimentary body within the post-Messinian succession that overlies unit 3 (Figure 4). It corresponds to unit 2 in Micallef et al. (2018) and is located adjacent to the base of the central and northern sections of the Malta Escarpment (Figures 4, 6, 7, 8). Unit 2 consists of acoustically chaotic to transparent seismic facies that displays vertical and lateral changes in seismic character. The internal configuration of the lower half of the unit is predominantly transparent, whereas the upper half shows stronger reflectivity with isolated landward or basinward dipping reflectors (Figures 6a-b, 8). Unit 2 has a wedge-shaped geometry that thins eastwards and southwards. It varies laterally from basin fill at the base of the Malta Escarpment, with discontinuous/chaotic to transparent reflectors that do not show clear internal seismic geometry, to a drape featuring intermediate amplitude and discontinuous reflectors on the gentle folds of the outer Calabrian accretionary wedge (Figure 6c). Unit 2 terminates abruptly against the Malta Escarpment. Unit 2 pinches out along its eastern and southern boundary (Figures 6c, 8). The top (horizon C) of unit 2 consist of high amplitude and irregular reflectors with the same polarity as the seafloor (Figures 4a, 6a, 9a).

Unit 2 covers an area of 13,600 km^2 (~100 km × 165 km) (Figures 7, 8). It is up to 0.68 s (two-way travel time (TWTT)) thick, which is equivalent to 790-890 m (estimated using pre-stack depth migration seismic velocities of 2300 and 2600 m/s, derived from seismic profiles CROP-21 and Archimede-16 (Gallais et al., 2013; Micallef et al., 2018). The point with the highest thickness is located between the mouth of Noto Canyon and the promontory on the Malta Escarpment. Unit 2 has a volume of 1477–1657 km^3.

4.1.3. Unit 1

In proximity to the Malta Escarpment, three clearly defined sub-units (units 1a-c) can be idenfied. Unit 1c is spatially coincident with unit 1b and it is difficult to identify as a distinct sub-unit where unit 1b does not occur. This is the case in the distal part of the study area, for example, which is characterised by tectonic deformation and a decrease in sediment thickness. As a result, where unit 1b is absent, units 1a and 1c have been combined into unit 1, which represents the entire period from 5.33 Ma to present (Figure 2c).

(a) Unit 1c

Above unit 2, three sedimentary deposits were mapped and are labelled as one unit - unit 1c - based on similarity of seismic facies (Figures 6a, 8, 9, 10a, 11). Unit 1c consists of a sequence of parallel to sub-parallel, continuous high amplitude reflectors. Because of the similarity to unit 1a (see section 4.1.3(c)), unit 1c is interpreted as Pliocene-Early Pleistocene units of hemipelagic, turbiditic and contouritic origin. The top (horizon B) of unit 1c is marked by a high amplitude reflector that is parallel to the internal reflections within unit 1c, and locally passes laterally to an erosional event that truncates unit 1c and unit 2 (Figures 9b, 10a), coinciding with the base of unit 1b. The base of unit 1c (horizon C) is a high amplitude reflection, parallel to the internal configuration of unit 1c, which corresponds to the top of unit 2. The boundary between unit 1c and the underlying unit 2 varies from onlap to concordant. The deposits in unit 1c are lenticular in cross-section; they have areas of 495, 325 and 55 km^2 and a thickness of up to 0.17 s (TWTT). This is equivalent to 150 m (Figure 11), if a pre-stack depth migration seismic velocity similar to that of unit 1a (1780 m/s) is assumed (Micallef et al., 2018). The total estimated volume of unit 1c is ~18 km^3.

(b) Unit 1b

Unit 1b, stratigraphically located above units 1c and 2, is a body with a chaotic to transparent seismic signature that has an estimated age of ~1.8 Ma (Figures 6a, 8, 9, 10, 12a-b). It is considerably thinner and smaller than unit 2 and occurs in the northern part of the study area, extending between the seafloor offshore Siracusa and the escarpment promontory to the south-east. The internal configuration of unit 1b is mainly transparent. Coherent reflectivity is sparse in the upper part of the unit, where reflectors with poor lateral continuity can be observed within a chaotic background. Unit 1b terminates abruptly or in onlap against the Malta Escarpment, and locally onlaps unit 2 (Figure 9b). Unit 1b has a wedge-shaped geometry that thins southwards and eastwards and forms a pinch-out termination (Figures 8, 9). The top (horizon A) and base (horizon B) of unit 1b consist of laterally continuous, high amplitude reflectors with the same polarity as the seafloor (Figures 6a, 9b). The base of unit 1b (horizon B) generally consists of a clear erosional truncation surface that coincides with the top of units 1c and 2.

The topography of the top of unit 1b shows a gentle slope gradient from north to south (Figure 12a).

Unit 1b covers an area of 2821 km^2 (75 km × 30 km) (Figures 8, 12a-b). It is up to 0.31 s (TWTT) thick, which is equivalent to 360-400 m, if a pre-stack depth migration seismic velocity similar to that of unit 2 (2300 and 2600 m/s) is assumed (Gallais et al., 2013; Micallef et al., 2018). The point with the highest thickness is located east of the mouth of Noto Canyon. Unit 1b has an estimated volume of 207-234 km^3.

(c) Unit 1a

Unit 1a is the uppermost unit in the western Ionian Basin and consists of a sequence of parallel, continuous, moderate to high amplitude reflectors that are locally sub-parallel, undulating or gently folded (Figures 4, 6, 9, 10). Unit 1a has been correlated to a mid-Pleistocene to Recent succession of hemipelagic, turbiditic and contouritic origin (Hieke et al., 2003; Micallef et al., 2019) with an increased terrigenous input (reflected in a higher sedimentation rate) with respect to the underlying unit 1c. It reaches a thickness of up to 0.720 s (TWTT), which is equivalent to 640 m, if a pre-stack depth migration seismic velocity of 1780 m/s is employed (Micallef et al., 2018). Nine sub-units with wedge-shaped geometry and variable thickness, consisting of acoustically chaotic to transparent reflector packages, were identified within unit 1a (Figures 6c, 8, 10a-b). They are up to 14 km in length and 0.26 s (TWTT) thick, and their age ranges between 1.6 and 0.4 Ma.

Unit 1a also includes >60 vertical seismic chimneys that are up to 25 m wide (Figures 6b, 8, 9, 10a). These chimneys extend from the top of unit 2 to the seafloor and disturb the lateral continuity of the seismic reflectors in unit 1.

4.2. Numerical simulations

Here we present the results of the 2-D hydraulic model simulations of the Zanclean flood and a minor and subsequent flood event, to assess if, and under which conditions, these could have emplaced the chaotic to transparent seismic facies in units 2 and 1b, respectively.

Figure 13a displays the resulting flow velocities in the steady-state, reached after 10 days, for the different simulations of the Zanclean flood considering the inflow boundary condition of 47.4 Sv (47.4 × 10^6 m^3/s) and eight independent sea level values (i.e. initial conditions) between -2400 and -1700 m in the western Ionian Basin. In all scenarios, the water from the western Mediterranean Basin flows into the eastern Mediterranean Basin via Noto Canyon. In the lower initial water values (-2400 to -2100 m), the flow is being obstructed by the positive topographic relief north of Alfeo Seamount. This obstruction produces bifurcation of the main flow in two preferential flows that run to the N/NW and S/SE. Two zones of low flow velocity are located in the shadow of these preferential flows and correspond to recirculation regions. The recirculating flow located to the south (RZ2) is considerably larger than that to the north (RZ1) (Table 1). At -2000 m initial water value, the water crosses the positive topographic relief north of Alfeo Seamount. This results in a change in the flood dynamics because it generates an additional flow path. In these conditions, the two recirculation areas have moved to the east and increased in size (Table 1). At -1900 m, the main body of the flood moves in a SW to NE direction. This change in the hydrodynamics directly affects the location of the reattachment point. The length and width of RZ1 change from 14.44 km and 6.74 km to 15.23 km and 11.5 km, respectively, in comparison with the -2000 m setting. In the case of RZ2, the length and width change from 27.71 km and 15.32 km to 75.91 km and 20.01 km, respectively (Table 1). The positive topographic relief north of Alfeo Seamount generates small wakes with low flow velocity (Figures 13a, 14a). A wake is a region of low velocity caused by the drag on an upstream body (Euler et al., 2017). The first reach of the wake is formed by two counterrotating vortices that develop at the back of the positive topographic relief (Figure 14a). For scenarios of -1800 m and -1700 m, the wakes disappear, and there is only an individual flow path from SW to NE (Figure 13a). Changes in the dimensions of the primary recirculation regions for these scenarios are minor. These flood dynamics are very similar to those for -1600 m and -1500 m, and for this reason the plots for the latter are not reproduced here.

Figure 13b shows the hydraulics of a putative second, smaller flood event with an initial water level of -900 m in the western Ionian Basin for different water flows of 5, 10, 15 and 20 Sv. The formation of two recirculation zones near the Malta Escarpment for the various water flows is observed. The flow velocity of the main pathway has values of 20-30 m/s. The results for an initial water level between -1200 and -500 m in western Ionian Basin show the same behaviour and are not reproduced here.

5. DISCUSSION

5.1 Unit 2 – Zanclean flood deposit

The following observations, made from the seismic reflection data, strengthen the previous interpretation by Micallef et al. (2018) that unit 2 is a deposit of material eroded and transported across the Pelagian Platform by the passage of the Zanclean flood from the western to the eastern Mediterranean basins:

(i) The basinward and landward dipping reflectors in unit 2 are reminiscent of sedimentary geometries reported onshore and interpreted as current structures produced by the advance and retreat of a flood (Benito et al., 2003; Waitt et al., 2019), although it should be noted that there is a significant difference in scale. This observation, combined with the transparent lower half and stronger reflectivity in the upper half of unit 2, suggest two stages of the sediment flow: a faster, advancing stage followed by a slower, retreating stage.
(ii) The lateral variation in seismic facies suggests that mass deposition was rapid and involved coarser material in the vicinity of the Malta Escarpment, whereas lower energy deposition involving finer-grained material took place with increasing distance towards the south and east.
(iii) The pinch-out terminations in the distal part of unit 2 suggest a gradual decrease in the energy of the flow and in the sediment supply.
(iv) The topography of the Messinian evaporite surface shows an extensive and elongate depression that partly matches the thickest section of unit 2. Across the northern part of the depression, the top of unit 3a has an irregular pattern. We therefore interpret this depression as a channel eroded by the Zanclean flood. An alternative explanation is that the depression was formed by subsidence in the underlying evaporites due to rapid deposition of the Zanclean flood deposit. If this were the case, however, the extent of the depression would exactly match the thickest section of unit 2.

(v) The seismic chimneys extending vertically upwards from the top of unit 2 into unit 1 are interpreted as fluid flow pathways, likely originating from dewatering from the rapidly emplaced flood deposit.

The results from the numerical modelling also provide additional support to the megaflood interpretation by Micallef et al. (2018). The modelled flood dynamics, specifically for the recirculation region RZ2, are compared with the isopach map of unit 2. The depositional processes are dominant above the stagnation point of the recirculating zone. The centroid of RZ2 is nearest to the maximum thickness of unit 2 for scenarios -1900 to -1700 m (Figures 7b, 13a; Table 2). The wakes forming in response to the positive topographic relief north of Alfeo Seamount in the -1900 m scenario correspond to zones of high sediment thickness in unit 2 (Figures 7b, 13a). Such wakes do not occur in the -1800 and -1700 m scenarios. The -1900 m scenario is, therefore, the best to explain the flow dynamics of the Zanclean flood. For this scenario, a good correspondence between the thickest part of unit 2 (>700 m) and the stagnation point location of RZ2 is observed (Figure 14a). The topological features of flow patterns in RZ1 agree with the geometry of a >400 m thick sedimentary body deposited to the north of the mouth of Noto Canyon.

The plots in Figure 15 (top panels) and the Hjulström diagram (Hjulstrom, 1935) are used to illustrate the correlation between the potential grain size of deposited sediment and water flows of 47.4, 25, 10 and 2 Sv (Figure 15, bottom panels). For the optimal value of 47.4 Sv, extensive zones of deposition in the recirculation regions RZ1 and RZ2 are observed. In the stagnation points, deposits include the finest sediment (0.2 mm (sands) to 20 mm (pebbles)). Adjacent to this area, velocities between 0.5 and 1 m/s correspond with deposition of a grain size of 20-100 mm (pebbles and cobbles). In the external zone of the vortices, the flow velocity increases to values of >1 m/s, depositing sediment with grain size of >100 mm (cobbles and boulders). In the wakes of the positive topographic relief north of Alfeo Seamount, the deposited material varies from sands to boulders. For water flows of 25 Sv and 10 Sv, a fining of the deposited sediment (from cobbles to sands) within the same zones is observed. At 2 Sv, deposition of sediment occurs across most of the computational domain. The finer sediment deposits are emplaced around the vortex cores and wakes. Near the separating streamlines and the remaining areas, deposition involves cobbles and boulders. There is high variability in terms of deposit grain size between the different simulated water flows. The vortex core is the zone that shows more uniformity between the different simulations and where the finest grain sizes are likely to have been deposited. In the rest of unit 2, the sedimentation process is likely to have been very variable.

Between the two recirculation regions, a higher flow velocity is observed, which corresponds to the main flow current (Figure 14a). These velocities (>30 m/s) are more compatible with erosive than depositional processes. Values of sediment thickness >400 m are reported in this section of unit 2 (Figures 7b, 14a). A plausible explanation is that such a sedimentary structure represents a three-dimensional landform under a supercritical flow condition. To test this hypothesis, we compared the isopach map of unit 2 and the simulated Froude number for the -1900 m sea level and 47.4 Sv streamflow (Figure 14b). The jet flow downstream of the Noto Canyon was supercritical but developed two sharp transitions to the subcritical regime upstream of the two topographic reliefs in the western Ionian Basin. The two bi-dimensional hydraulic jumps, denoted by HJ1 and HJ2 in Figures 3c and 14b, are 60 m in depth. Interestingly, their nonlinear interaction leads to an abrupt variation in the Froude number over the thickest deposit. The Froude parameter reaches a maximum of 4 inside the area delimited by the highest sediment-thickness level. Both in the mainstream and transverse sections crossing the maximum thickness, the Froude number drops below 2. Such non-uniform flow conditions could have induced mass deposition because of spatial variations in the sediment transport capacity.

5.2 Unit 1b – Mass movement deposit

The seismic character and geometry of unit 1b is similar to that of unit 2, suggesting an origin related to either a second flood event or a submarine slope instability.

The first scenario would suggest that the Zanclean flood potentially comprised two flood events, including a volumetrically larger one forming unit 2, followed by a smaller one depositing unit 1b. There are a number of problems with this interpretation, however:

(i) The outcomes of the overtopping megaflood model (Garcia-Castellanos et al., 2009) strongly argue against multiple flooding events, for two reasons. First they suggest that a slow flood is only possible in the very beginning of the Atlantic overtopping through the Strait of Gibraltar, and only for duration of ~3 ka at most, which leaves no time for a potential deposition of unit 1c as turbiditic and hemipelagic sediments in between the two flood events. Second, the flood process soon becomes irreversible because as erosion excavates a deeper inlet, it inevitably leads to discharge rates above 1 Sv, with most of the flood volume discharging into the Mediterranean Sea at rates above 40 Sv. Such fast flood erosion outpacing any vertical sea level or tectonic motions is at odds with the occurrence of multiple floods or even with an intermediate calm period during which unit 1c can be deposited.

(ii) The interpretation of two floods with enough time in between to deposit unit 1c would imply a second disconnection from the ocean and a second evaporative drawdown, which in turn implies a renewed phase of tectonic uplift in Gibraltar that closes the gateway for a second time. This second desiccation should trigger additional isolation of the Mediterranean Sea due to the isostatic rebound of the Strait of Gibraltar (Coulson et al., 2019; Garcia-Castellanos and Villaseñor, 2011; Govers, 2009). Therefore, subsequent subsidence or sea level rise in the Atlantic would be required to allow a second, smaller flood. This scenario is complicated, unreasonable from a geodynamic point of view (Garcia-Castellanos et al., 2009), and unsupported by other data.

(iii) Recent work has called into question the two-stage flooding models proposed by Bache et al. (2009, 2012). The rates of Mediterranean Sea level rise, estimated by Periáñez et al. (2019) using a 2-D hydrodynamic model, confirm values obtained by Garcia-Castellanos et al. (2009) reaching up to 10 m/day. These rates are incompatible with the formation of a wave ravinement, which is at the foundation of the two-stage flooding models (Bache et al., 2009). In addition, the current generated by the flood is not strong enough enough to erode such ravinement surfaces. The shear stress of the flow drastically reduces towards the shores of the ever-rising Mediterranean lakes (Periáñez et al., 2019), and the coastal areas are prone to sedimentation of the materials carried by the megaflood, rather than erosion. Similar erosive terraces along the Malta Escarpment, for example, have been attributed to coastal erosion during extended base-level fall (Micallef et al., 2019).

(iv) Our 2-D numerical simulation results of a theoretical second flood event for 5, 10, 15 and 20 Sv show flow velocities of 2-30 m/s in correspondence with unit 1b (Figure 13b). These simulated velocities are incompatible with the deposition of this sedimentary body.

(v) Finally, the extrapolation of the Ionian basin sedimentation rate curve clearly indicates that unit 1b has been deposited long after the onset of the Zanclean Period. In our age model, the age of deposition of unit 1b should be about 1.8 Ma (Figure 2).

In view of the above considerations, a more likely origin for unit 1b is post-flood, submarine slope failure. The magnitude of the slope failure represented by unit 1b is unique in the post-Messian sedimentary history in the area. Such an event would account for the chaotic to transparent facies and the wedge shaped geometry of unit 1b, and the erosion, as indicated by truncated seismic reflectors, along the top of the underlying unit 1c. The volume of unit 1b also compares well with the volume of the northern tributary of Noto Canyon, which has a volume of ~200 km^3. A scar is still discernible upslope of the Noto Canyon (Figure 12c), although the original morphology is likely buried underneath sediment. The failure of the Noto Canyon head, possibly weakened by rapid erosion during the Zanclean flood, is the most likely source of material in unit 1b.

5.3 Chaotic sub-units in unit 1a – Mass movement deposits

The nine sub-units of chaotic to transparent seismic facies in the upper section of unit 1a (Figures 6c, 8, 10b) are interpreted as minor mass transport deposits. The majority of these are located adjacent to the Malta Escarpment and occurred between 1.6 and 0.4 Ma. The material for the mass transport deposits could have been sourced from the scars mapped by Micallef et al. (2019). The mobilised sediment is likely stratified, fine-grained contouritic or hemipelagic/pelagic sediments deposited across the Malta Escarpment canyon walls and heads (Micallef et al., 2019). The timing of the slope instability events is interpreted as a reponse of the margin to the gradual shift from low-amplitude 41 ka obliquity-driven periodicty of eustatic sea level changes to high-amplitude 100 ka eccentricity-driven changes during the so-colled Mid-Pleistocene climatic transition (e.g. Willeit et al. 2019). The margin to the west of the study area (Sicily and Pelagian Platform) became increasingly exposed for longer times during glacial periods, resulting in an increased extension of subaerial drainage systems across the continental shelf and upper slope during lowstands, and loading of slope sediments due to the direct discharge of terrigenous sediments. The occurrence of three megaturbidites in the Late Pleistocene succession of the Ionian abyssal plain, described by Hieke and Werner (2000), reflects the same trend, with a lower number of events in such a distal depositional setting.

5.4 Stratigraphic evolution of the western Ionian Basin

Based on the above inferences, the interpreted sequence of events that controlled the stratigraphic evolution of the western Ionian Basin includes the following (Figure 2c):

(i) Deposition of evaporites (unit 3) during the MSC (5.97 - 5.33 Ma);
(ii) Instantaneous emplacement of Zanclean flood deposit (unit 2) at the end of the MSC;
(iii) Deposition of turbiditic and hemipelagic sediments from 5.33 Ma to present (unit 1);
(iv) Failure of the Noto Canyon head and instantaneous emplacement of a large mass transport deposit (unit 1b) at ~1.8 Ma;
(v) Episodic failure of the Malta Escarpment and emplacement of mass transport deposits in response to increased magnitude of eustatic sea level changes between 1.6 and 0.4 Ma.

6. CONCLUSIONS

In this study, geophysical data from the western Ionian Basin and numerical modelling evidence demonstrate that:

(i) The termination of the MSC in the eastern Mediterranean Basin consisted of a single Zanclean flood.
(ii) The extensive sedimentary body with a chaotic to transparent seismic signature at the base of the Malta Escarpment (unit 2) can best be explained by deposition during the Zanclean flood, which corroborates the inference made by Micallef et al. (2018).
(iii) Fine, well-sorted sediments are predicted to have been deposited within the thicker sections of the flood deposit, which coincide with recirculating flows and wakes, whereas a more variable distribution of coarser sediments is expected elsewhere.
(iv) The flow dynamics of the Zanclean flood with a 1900 m drawdown during the MSC in the eastern Mediterranean best explain the observed distribution of unit 2 in the western Ionian Basin. This agrees with inferences, based on seafloor geomorphic evidence, made by Micallef et al. (2019).
(v) The north-western Ionian Basin shows evidence of episodic slope instability events. The majority of the mass movement deposits are small in volume and occurred after ~1.8 Ma. The largest deposit (>200 km^3) was likely emplaced by failure of the Noto Canyon head at ~1.8 Ma.

The identification of the Zanclean flood deposits is currently based on seismic imaging, numerical modelling, and their analogy with outcrop studies. Scientific drilling is thus needed to ground-truth their nature and stratigraphic position, and to support their link with the restricted influx of Atlantic water into the Mediterranean during the MSC and with the Zanclean reflooding events in the western Mediterranean Basin.

7. DATA AVAILABILITY

The multibeam echosounder data, and the multichannel seismic reflection profiles (from MS, CROP, CIRCEE-HR, CUMECS-3) data are available from the authors upon reasonable request. The multichannel seismic reflection profiles from CA-99 and MEM-07 are available from SPECTRUM (now TGS) but restrictions apply to the availability of these data, which were used under license for the current study, and so are not publicly available. Data are thus available from the corresponding author upon reasonable request and with permission of SPECTRUM (now TGS).

8. ACKNOWLEDGMENTS

The article is based upon work from COST Action CA15103 "Uncovering the Mediterranean salt giant" (MEDSALT) supported by COST (European Cooperation in Science and Technology). We are indebted to the CUMECS-2, CUMECS-3 and CIRCEE-HR shipboard parties, captains, crew and technicians for their assistance during data collection. The oceanographic surveys were possible following permits issued by the Italian and Maltese authorities. SPECTRUM (now TGS) are kindly acknowledged for providing access to their seismic reflection data. The use of CROP seismic profiles has been licensed to OGS by CNR, Banca Dati CROP (www.crop.cnr.it). The authors would also like to thank Emerson Paradigm for the use of the OGS academic licenses of the ECHOS and Geodepth processing software, and IHS Markit for the OGS license of the Kingdom software. DS is funded by EMODnet Bathymetry, which is financed by the European Union under Regulation 508/2014 of the European Parliament and of the Council of 15 May 2014 on the European Maritime and

Fisheries Fund. This work was also supported by the Spanish Ministry of Science, Innovation and Universities (MICINN/FEDER, EU) under Grant SEDRETO CGL2015-70736-R. J.D.d.M.E. was supported by the PhD scholarship BES-2016-079117 (MINECO/FSE, EU) from the Spanish National Programme for the Promotion of Talent and its Employability (call 2016). This project has received funding from the European Union's Horizon 2020 research and innovation programme under the Marie Skłodowska-Curie grant agreement No 765256 (SaltGiant ITN). We thank Marina Rabineau and an anonymous reviewer for their constructive comments.

9. REFERENCES

Abril, J.M., Periáñez, R., 2016. Revisiting the time scale and size of the Zanclean flood of the Mediterranean (5.33 Ma) from CFD simulations. Mar. Geol. 382, 242–256. https://doi.org/10.1016/j.margeo.2016.10.008

Adam, J., Reuther, C.D., Grasso, M., Torelli, L., 2000. Active fault kinematics and crustal stresses along the Ionian margin of southeastern Sicily. Tectonophysics 326, 217–239. https://doi.org/10.1016/S0040-1951(00)00141-4

Argnani, A., Bonazzi, C., 2005. Malta Escarpment fault zone offshore eastern Sicily: Pliocene-quaternary tectonic evolution based on new multichannel seismic data. Tectonics 24. https://doi.org/10.1029/2004TC001656

Bache, F., Olivet, J.L., Gorini, C., Rabineau, M., Baztan, J., Aslanian, D., Suc, J.P., 2009. Messinian erosional and salinity crises: View from the Provence Basin (Gulf of Lions, Western Mediterranean). Earth Planet. Sci. Lett. 286, 139–157. https://doi.org/10.1016/j.epsl.2009.06.021

Bache, F., Popescu, S.M., Rabineau, M., Gorini, C., Suc, J.P., Clauzon, G., Olivet, J.L., Rubino, J.L., Melinte-Dobrinescu, M.C., Estrada, F., Londeix, L., Armijo, R., Meyer, B., Jolivet, L., Jouannic, G., Leroux, E., Aslanian, D., Reis, A.T. Dos, Mocochain, L., Dumurdžanov, N., Zagorchev, I., Lesić, V., Tomić, D., Namik Çağatay, M., Brun, J.P., Sokoutis, D., Csato, I., Ucarkus, G., Çakir, Z., 2012. A two-step process for the reflooding of the Mediterranean after the Messinian Salinity Crisis. Basin Res. 24, 125–153. https://doi.org/10.1111/j.1365-2117.2011.00521.x

Baker, V.R., 2020. Global Megaflood Paleohydrology, in: Herget J., Fontana A. (Eds.), . Palaeohydrology. Geography of the Physical Environment. Springer, Cham, pp. 3–28. https://doi.org/10.1007/978-3-030-23315-0_1

Barber, P.M., 1981. Messinian subaerial erosion of the proto-Nile Delta. Mar. Geol. 44, 253–272

Ben-Avraham, Z., Grasso, M., 1991. Crustal structure variations and transcurrent faulting at the eastern and western margins of the eastern Mediterranean. Tectonophysics 196, 269–277. https://doi.org/10.1016/0040-1951(91)90326-N

Ben-Gai, Y., Ben-Avraham, Z., Buchbinder, B., Kendall, C.G.S.C., 2005. Post-Messinian evolution of the Southeastern Levant Basin based on two-dimensional stratigraphic simulation. Mar. Geol. 221, 359–379

Benito, G., Sánchez-Moya, Y., Sopena, A., 2003. Sedimentology of high-stage flood deposits of the Tagus River, Central Spain. Sediment. Geol. 157, 107–132. https://doi.org/10.1016/S0037-0738(02)00196-3

Bertoni, C., Cartwright, J.A., 2005. 3D seismic analysis of circular evaporite dissolution structures, Eastern Mediterranean. J. Geol. Soc. London. 162, 909–926. https://doi.org/10.1144/0016-764904-126

Biju-Duval, B., Morel, Y., Baudrimont, A., Bizon, G., Bizon, J.J., 2006. Données nouvelles sur les marges du Bassin Ionien profond (Méditerranée Orientale). Résultats des campagnes Escarmed. Rev. l'Institut Français du Pétrole 37, 713–730. https://doi.org/10.2516/ogst:1982036

Blanc, P.L., 2002. The opening of the Plio-Quaternary Gibraltar Strait: Assessing the size of a cataclysm. Geodin. Acta 15, 303–317. https://doi.org/10.1016/S0985-3111(02)01095-1

Blanc, P.L., 2000. Of sills and straits: A quantitative assessment of the Messinian Salinity Crisis. Deep. Res. Part I Oceanogr. Res. Pap. 47, 1429–1460. https://doi.org/10.1016/S0967-0637(99)00113-2

Blayo, E., Debreu, L., 2005. Revisiting open boundary conditions from the point of view of characteristic variables. Ocean Model. 9, 231–252.

Bohorquez, P., Cañada-Pereira, P., Jimenez-Ruiz, P.J., del Moral-Erencia, J.D., 2019. The fascination of a shallow-water theory for the formation of megaflood-scale dunes and antidunes. Earth-Science Rev. 193, 91–108. https://doi.org/10.1016/j.earscirev.2019.03.021

Camerlenghi, A., Del Ben, A., Hübscher, C., Forlin, E., Geletti, R., Brancatelli, G., Micallef, A., Saule, M., Facchin, L., 2019. Seismic markers of the Messinian salinity crisis in the deep Ionian Basin. Basin Res. https://doi.org/DOI: 10.1111/bre.12392

Carminati, E., Doglioni, C., Barba, S., 2004. Reverse migration of seismicity on thrusts and normal faults. Earth-Science Rev. 65, 195–222. https://doi.org/10.1016/S0012-8252(03)00083-7

Carrivick, J.L., 2006. Application of 2D hydrodynamic modelling to high-magnitude outburst floods: An example from Kverkfjöll, Iceland. J. Hydrol. 321, 187–199. https://doi.org/10.1016/j.jhydrol.2005.07.042

Catalano, R., Doglioni, C., Merlini, S., 2000. On the Mesozoic Ionian Basin. Geophys. J. Int. 143, 1–24. https://doi.org/10.1046/j.0956-540X.2000.01287.x

Cernobori, L., Hirn, A., McBride, J.H., Nicolich, R., Petronio, L., Romanelli, M., 1996. Crustal image of the Ionian basin and its Calabrian margins. Tectonophysics 264, 175–198. https://doi.org/10.1016/S0040-1951(96)00125-4

Coulson, S., Pico, T., Austermann, J., Powell, E., Moucha, R., Mitrovica, J.X., 2019. The role of isostatic adjustment and gravitational effects on the dynamics of the Messinian salinity crisis. Earth Planet. Sci. Lett. 525, 115760. https://doi.org/10.1016/j.epsl.2019.115760

Dannowski, A., Kopp, H., Klingelhoefer, F., Klaeschen, D., Gutscher, M.A., Krabbenhoeft, A., Dellong, D., Rovere, M., Graindorge, D., Papenberg, C., Klaucke, I., 2019. Ionian Abyssal Plain: A window into the Tethys oceanic lithosphere. Solid Earth 10, 447–462. https://doi.org/10.5194/se-10-447-2019

Del Ben, A., Geletti, R., Mocnik, A., 2010. Relation between recent tectonics and inherited Mesozoic structures of the central-southern Adria plate. Boll. di Geofis. Teor. ed Appl. 51, 99-115

Dellong, D., Klingelhoefer, F., Kopp, H., Graindorge, D., Margheriti, L., Moretti, M., Murphy, S., Gutscher, M.A., 2018. Crustal Structure of the Ionian Basin and Eastern Sicily Margin: Results From a Wide-Angle Seismic Survey. J. Geophys. Res. Solid Earth 123, 2090–2114. https://doi.org/10.1002/2017JB015312

Druckman, Y., Buchbinder, B., Martinotti, G.M., Tov, R.S., Aharon, P., 1995. The buried Afiq Canyon (eastern Mediterranean, Israel): a case study of a Tertiary submarine canyon exposed in Late Messinian times. Mar. Geol. 123, 167–185.

Esteras, M., Izquierdo, J., Sandoval, N.G., Mamad, A., 2000. Evolución morfológica y estratigráfica pliocuaternaria del umbral de Camarinal (Estrecho de Gibraltar) basada en sondeos marinos. Rev. Soc. Geol. España 13, 539–550

Estrada, F., Ercilla, G., Gorini, C., Alonso, B., Vázquez, J.T., García-Castellanos, D., Juan, C., Maldonado, A., Ammar, A., Elabbassi, M., 2011. Impact of pulsed Atlantic water inflow into the Alboran Basin at the time of the Zanclean flooding. Geo-Marine Lett. 31, 361–

376. https://doi.org/10.1007/s00367-011-0249-8
Euler, T., Herget, J., Schlomer, O., Benito, G., 2017. Hydromorphological processes at submerged solitary boulder obstacles in streams. Catena 157, 250-267
Finetti, I., 1982. Structure, stratigraphy and evolution of central Mediterranean (Pelagian Sea, Ionian Sea). Boll. di Geofis. Teor. ed Appl. 24, 247–312. https://doi.org/10.1007/s10539-010-9244-0
Finetti, I.R., Del Ben, A., Fais, S., Forlin, E., Klingelé, E., Lecca, L., Pipan, M., Prizzon, A., 2005. Crustal Tectono-Stratigraphic Setting of the Pelagian Foreland from the New CROP Seismic Data, in: CROP Project - Deep Seismic Explanation of the Central Mediterranean and Italy. pp. 581–596
Flecker, R., Krijgsman, W., Capella, W., de Castro Martíns, C., Dmitrieva, E., Mayser, J.P., Marzocchi, A., Modestu, S., Ochoa, D., Simon, D., Tulbure, M., van den Berg, B., van der Schee, M., de Lange, G., Ellam, R., Govers, R., Gutjahr, M., Hilgen, F., Kouwenhoven, T., Lofi, J., Meijer, P., Sierro, F.J., Bachiri, N., Barhoun, N., Alami, A.C., Chacon, B., Flores, J.A., Gregory, J., Howard, J., Lunt, D., Ochoa, M., Pancost, R., Vincent, S., Yousfi, M.Z., 2015. Evolution of the Late Miocene Mediterranean-Atlantic gateways and their impact on regional and global environmental change. Earth-Science Rev. 150, 365–392. https://doi.org/10.1016/j.earscirev.2015.08.007
Gallais, F., Graindorge, D., Gutscher, M.A., Klaeschen, D., 2013. Propagation of a lithospheric tear fault (STEP) through the western boundary of the Calabrian accretionary wedge offshore eastern Sicily (Southern Italy). Tectonophysics 602, 141–152. https://doi.org/10.1016/j.tecto.2012.12.026
Garcia-Castellanos, D., Estrada, F., Jiménez-Munt, I., Gorini, C., Fernández, M., Vergés, J., De Vicente, R., 2009. Catastrophic flood of the Mediterranean after the Messinian salinity crisis. Nature 462, 778–781. https://doi.org/10.1038/nature08555

Garcia-Castellanos, D., Micallef, A., Estrada, F., Camerlenghi, A., Ercilla, G., Periáñez, R., Abril, J.M., 2020. The Zanclean megaflood of the Mediterranean–Searching for independent evidence. Earth-Science Rev. 201, 103061.

Garcia-Castellanos, D., Villaseñor, A., 2011. Messinian salinity crisis regulated by competing tectonics and erosion at the Gibraltar arc. Nature 480, 359–363. https://doi.org/10.1038/nature10651

García-Feal, O., González-Cao, J., Gómez-Gesteira, M., Cea, L., Domínguez, J.M., Formella, A., 2018. An accelerated tool for flood modelling based on Iber. Water (Switzerland) 10, 1459. https://doi.org/10.3390/w10101459

Gargani, J., Rigollet, C., 2007. Mediterranean Sea level variations during the Messinian salinity crisis. Geophys. Res. Lett. 34, L10405

Gennari, R., Manzi, V., Angeletti, L., Bertini, A., Biffi, U., Ceregato, A., Faranda, C., Gliozzi, E., Lugli, S., Menichetti, E., Rosso, A., Roveri, M., Taviani, M., 2013. A shallow water record of the onset of the Messinian salinity crisis in the Adriatic foredeep (Legnagnone section, Northern Apennines). Palaeogeogr. Palaeoclimatol. Palaeoecol. 386, 145–164. https://doi.org/10.1016/j.palaeo.2013.05.015

Govers, R., 2009. Choking the Mediterranean to dehydration: The Messinian salinity crisis. Geology 37, 167–170. https://doi.org/10.1130/G25141A.1

Govers, R., Wortel, M.J.R., 2005. Lithosphere tearing at STEP faults: Response to edges of subduction zones. Earth Planet. Sci. Lett. 236, 505–523. https://doi.org/10.1016/j.epsl.2005.03.022

Gutscher, M.A., Dominguez, S., De Lepinay, B.M., Pinheiro, L., Gallais, F., Babonneau, N., Cattaneo, A., Le Faou, Y., Barreca, G., Micallef, A., Rovere, M., 2016. Tectonic expression of an active slab tear from high-resolution seismic and bathymetric data offshore Sicily (Ionian Sea). Tectonics 35, 39–54. https://doi.org/10.1002/2015TC003898

Gutscher, M.A., Kopp, H., Krastel, S., Bohrmann, G., Garlan, T., Zaragosi, S., Klaucke, I., Wintersteller, P., Loubrieu, B., Le Faou, Y., San Pedro, L., Dominguez, S., Rovere, M., Mercier de Lepinay, B., Ranero, C., Sallares, V., 2017. Active tectonics of the Calabrian subduction revealed by new multi-beam bathymetric data and high-resolution seismic profiles in the Ionian Sea (Central Mediterranean). Earth Planet. Sci. Lett. 461, 61–72. https://doi.org/10.1016/j.epsl.2016.12.020

Haq, B., Gorini, C., Baur, J., Moneron, J., Rubino, J.-L., 2020. Deep Mediterranean's Messinian evaporite giant: How much salt? Glob. Planet. Change 184, 103052. https://doi.org/https://doi.org/10.1016/j.gloplacha.2019.103052

Hieke, W., Hirschleber, H.B., Dehghani, G.A., 2003. The Ionian Abyssal Plain (central Mediterranean Sea): Morphology, subbottom structures and geodynamic history–an inventory. Mar. Geophys. Res. 24, 279–310

Hieke, W., Werner, F., 2000. The Augias megaturbidite in the central Ionian Sea (central Mediterranean) and its relation to the Holocene Santorini event. Sediment. Geol. 135, 205–218

Hjulstrom, F., 1935. Studies of the morphological activity of rivers as illustrated by the River Fyris, Bulletin. Geol. Inst. Upsalsa 25, 221–527

Hsü, K.J., Montard, L., Garrison, R.B., Fabricius, F.H., Kidd, R.B., Müller, C., Cita, M.B., Bizon, G., Wright, R.C., Erickson, A.J., 1978. Site 374 : Messina Abyssal Plain. Initial Rep. Deep Sea Drill. Proj, 42, 175–217. https://doi.org/10.1017/CBO9781107415324.004

Jongsma, D., van Hinte, J.E., Woodside, J.M., 1985. Geologic structure and neotectonics of the North African Continental Margin south of Sicily. Mar. Pet. Geol. 2, 156–179. https://doi.org/10.1016/0264-8172(85)90005-4

Krijgsman, W., Stoica, M., Vasiliev, I., Popov, V. V., 2010. Rise and fall of the Paratethys Sea during the Messinian Salinity Crisis. Earth Planet. Sci. Lett. 290, 183–191.

https://doi.org/10.1016/j.epsl.2009.12.020

Lofi, J., 2002. La crise de salinité messinienne: conséquences directes et différées sur l'évolution sédimentaire de la marge du Golfe du Lion

Lofi, J, Déverchère, J., Gaullier, V., Gillet, H., Gorini, C., Guennoc, P., Loncke, L., Maillard, A., Sage, F., Thinon, I., World, C. for the G.M. of the, 2011. Seismic Atlas of the Messinian Salinity Crisis markers in the Mediterranean and Black Seas. Mem. la Société Géologique Fr.

Lofi, Johanna, Sage, F., Deverchere, J., Loncke, L., Maillard, A., Gaullier, V., Thinon, I., Gillet, H., Guennoc, P., Gorini, C., 2011. Refining our knowledge of the Messinian salinity crisis records in the offshore domain through multi-site seismic analysis. Bull. la Soc. Geol. Fr. 182(2), 163–180. https://doi.org/10.2113/gssgfbull.182.2.163

Lugli, S., Manzi, V., Roveri, M., Schreiber, B.C., 2015. The deep record of the Messinian salinity crisis: Evidence of a non-desiccated Mediterranean Sea. Palaeogeogr. Palaeoclimatol. Palaeoecol. 433, 201–218. https://doi.org/10.1016/j.palaeo.2015.05.017

Madof, A.S., Bertoni, C., Lofi, J., 2019. Discovery of vast fluvial deposits provides evidence for drawdown during the late Miocene Messinian salinity crisis. Geology 47(2), 171–174. https://doi.org/10.1130/G45873.1

Maesano, F.E., Tiberti, M.M., Basili, R., 2017. The Calabrian Arc: Three-dimensional modelling of the subduction interface. Sci. Rep. 7, 8887. https://doi.org/10.1038/s41598-017-09074-8

Maillard, A., Mauffret, A., 1993. Structure et volcanisme de la fosse de Valence (Méditerranée nord-occidentale). Bull. la Société Géologique Fr. 164, 365–383

Mantovani, E., Viti, M., Babbucci, D., Albarello, D., 2007. Nubia-Eurasia kinematics: An alternative interpretation from Mediterranean and North Atlantic evidence. Ann. Geophys. 50(3), 341–366

Marzocchi, A., Flecker, R., van Baak, C.G.C., Lunt, D.J., Krijgsman, W., 2016. Mediterranean outflow pump: An alternative mechanism for the Lago-mare and the end of the Messinian Salinity Crisis. Geology 44, 523–526. https://doi.org/10.1130/G37646.1

Max, M.D., Kristensen, A., Michelozzi, E., 1993. Small scale Plio-Quaternary sequence stratigraphy and shallow geology of the west-central Malta Plateau. Geol. Dev. Sicil. Platf. 117–122

Meilijson, A., Hilgen, F., Sepúlveda, J., Steinberg, J., Fairbank, V., Flecker, R., Waldmann, N.D., Spaulding, S.A., Bialik, O.M., Boudinot, F.G., Illner, P., Makovsky, Y., 2019. Chronology with a pinch of salt: Integrated stratigraphy of Messinian evaporites in the deep Eastern Mediterranean reveals long-lasting halite deposition during Atlantic connectivity. Earth-Science Rev. 194, 374–398. https://doi.org/10.1016/j.earscirev.2019.05.011

Micallef, A., Berndt, C., Debono, G., 2011. Fluid flow systems of the Malta Plateau, Central Mediterranean Sea. Mar. Geol. 284, 74–85. https://doi.org/10.1016/j.margeo.2011.03.009

Micallef, A., Camerlenghi, A., Garcia-Castellanos, D., Cunarro Otero, D., Gutscher, M.-A.M.A., Barreca, G., Spatola, D., Facchin, L., Geletti, R., Krastel, S., Gross, F., Urlaub, M., Micallef, A., Sulli, A., Basilone, L., Basilone, G., 2018. Evidence of the Zanclean megaflood in the eastern Mediterranean Basin. Sci. Rep. 8, 1–8. https://doi.org/10.1038/s41598-018-19446-3

Micallef, A., Camerlenghi, A., Georgiopoulou, A., Garcia-Castellanos, D., Gutscher, M.-A., Lo Iacono, C., Huvenne, V.A.I., Mountjoy, J.J., Paull, C.K., Le Bas, T., Spatola, D., Facchin, L., Accettella, D., 2019. Geomorphic evolution of the Malta Escarpment and implications for the Messinian evaporative drawdown in the eastern Mediterranean Sea. Geomorphology 327, 264–283. https://doi.org/10.1016/j.geomorph.2018.11.012

Micallef, A., Georgiopoulou, A., Mountjoy, J., Huvenne, V.A.I., Iacono, C. Lo, Le Bas, T., Del Carlo, P., Otero, D.C., 2016. Outer shelf seafloor geomorphology along a carbonate escarpment: The eastern Malta Plateau, Mediterranean Sea. Cont. Shelf Res. 131, 12–27. https://doi.org/10.1016/j.csr.2016.11.002

Osler, J.C., Algan, O., 1999. A high resolution seismic sequence analysis of the Malta Plateau. NATO. SACLANTCEN.

Periáñez, R., Abril, J.M., Garcia-Castellanos, D., Estrada, F., Ercilla, G., 2019. An exploratory modelling study on sediment transport during the Zanclean flood of the Mediterranean. SN Appl. Sci. 1, 364. https://doi.org/10.1007/s42452-019-0374-y

Pellen, R., Aslanian, D., Rabineau, M., Suc, J.P., Gorini, C., Leroux, E., Blanpied, C., Silenziario, C., Popescu, S.M., Rubino, J.L., 2019. The Messinian Ebro River incision. Global Planet. Change 181, 102988

Polonia, A., Vaiani, S.C., De Lange, G.J., 2016. Did the A.D. 365 Crete earthquake/tsunami trigger synchronous giant turbidity currents in the Mediterranean Sea? Geology 44, 19–22. https://doi.org/10.1130/G37486.1

Rouchy, J.M., Caruso, A., 2006. The Messinian salinity crisis in the Mediterranean basin: A reassessment of the data and an integrated scenario. Sediment. Geol. 188–189, 35–67. https://doi.org/10.1016/j.sedgeo.2006.02.005

Roveri, M., Bassetti, M.A., Ricci Lucchi, F., 2001. The mediterranean Messinian salinity crisis: An Apennine foredeep perspective. Sediment. Geol. 140, 201–214. https://doi.org/10.1016/S0037-0738(00)00183-4

Roveri, M., Flecker, R., Krijgsman, W., Lofi, J., Lugli, S., Manzi, V., Sierro, F.J., Bertini, A., Camerlenghi, A., De Lange, G., Govers, R., Hilgen, F.J., Hübscher, C., Meijer, P.T., Stoica, M., 2014. The Messinian Salinity Crisis: Past and future of a great challenge for marine sciences. Mar. Geol. 352, 25–58. https://doi.org/10.1016/j.margeo.2014.02.002

Ryan, W.B.F., 2009. Decoding the mediterranean salinity crisis. Sedimentology 56, 95–136.

https://doi.org/10.1111/j.1365-3091.2008.01031.x
Ryan, W.B.F., 1976. Quantitative evaluation of the depth of the western Mediterranean before, during and after the Late Miocene salinity crisis. Sedimentology 23, 791–813
San Pedro, L., Babonneau, N., Gutscher, M.A., Cattaneo, A., 2017. Origin and chronology of the Augias deposit in the Ionian Sea (Central Mediterranean Sea), based on new regional sedimentological data. Mar. Geol. 384, 199–213. https://doi.org/10.1016/j.margeo.2016.05.005
Scandone, P., 1981. Mesozoic and Cenozoic rocks from the Malta Escarpment (central Mediterranean). Am. Assoc. Pet. Geol. Bull. 65, 1299–1319. https://doi.org/10.1306/03B5949F-16D1-11D7-8645000102C1865D
Selli, R., 1954. Il bacino del Metauro: descrizione geologica, risorse minerarie, idrogeologia. Museo geologico Giovanni Cappellini
Shipboard Scientific Party, 1978. Site 374, Messina Abyssal Plain. In Hsü, K. J., Montadert, L., et al., 1978. Initial Reports of the Deep Sea Drilling Project, Volume 42, Part 1: Washington (U.S. Government Printing Office), pp. 175-217
Shipboard Scientific Party, 1996. Site 964. In Emeis, K.-C, Robertson, A.H.F., Richter, C, et al., Proc. ODP, Init. Repts., 160: College Station, TX (Ocean Drilling Program), 85-123
Speranza, F., Minelli, L., Pignatelli, A., Chiappini, M., 2012. The Ionian Sea: The oldest in situ ocean fragment of the world? J. Geophys. Res. B Solid Earth 117. https://doi.org/10.1029/2012JB009475
Stampfli, G.M., Höcker, C.F.W., 1989. Messinian paleorelief from a 3-D seismic survey in the Tarraco concession area (Spanish Mediterranean Sea). Geol. Mijnb. 68, 201–210
Steckler, M.S., Lofi, J., Mountain, G.S., Ryan, W.B.F., Berné, S., Gorini, C., 2003. Reconstruction of the Gulf of Lions margin during the Messinian Salinity Crisis, in: EGS-AGU-EUG Joint Assembly

Tibor, G., Ben-Avraham, Z., 2005. Late Tertiary paleodepth reconstruction of the Levant margin off Israel. Mar. Geol. 221, 331–347

Urgeles, R., Camerlenghi, A., Garcia-Castellanos, D., De Mol, B., Garcés, M., Vergés, J., Haslam, I., Hardman, M., 2011. New constraints on the Messinian sealevel drawdown from 3D seismic data of the Ebro Margin, western Mediterranean. Basin Res. 23, 123–145

Van Couvering, J. a., Castradori, D., Cita, M.B., Hilgen, F.J., Rio, D., 1971. The base of the Zanclean Stage and of the Pliocene Series. Episodes 23, 179–187

Waitt, A.R.B., Long, W.A., Stanton, K.M., 2019. Erratics and Other Evidence of Late Wisconsin Missoula Outburst Floods in Lower Wenatchee and Adjacent Columbia Valleys , Washington Erratics and Other Evidence of Late Wisconsin Missoula Outburst Floods in Lower Wenatchee and Adjacent Columbia Valleys, Bione Complet. 92, 318–337

Weijermars, R., 1988. Neogene tectonics in the Western Mediterranean may have caused the Messinian salinity crisis and an associated glacial event. Tectonophysics 148, 211–219. https://doi.org/10.1016/0040-1951(88)90129-1

Willeit, M., Ganopolski, A., Calov, R., Brovkin, V., 2019. Mid-Pleistocene transition in glacial cycles explained by declining CO_2 and regolith removal. Sci. Adv. 5, eaav7337.

10. TABLE CAPTIONS

Table 1: Width and height of recirculation zones RZ1 and RZ2 for different pre-flood water level scenarios.

Table 2: Location and displacement (in WGS84 datum) of the centre point of RZ2 with respect to the zone of maximum thickness of unit 2, for different pre-flood water level scenarios.

11. FIGURE CAPTIONS

Figure 1: Bathymetric map of the eastern margin of the Pelagian Platform and western Ionian Basin. The map displays the principal morphological and structural features, and the spatial coverage of the multi-channel seismic reflection data. Location of figures 4a, 6a, 6c, 9a, 10a and 10b, and holes ODP 964 and DSDP 374, is indicated.

Figure 2: Stratigraphic scheme for the western Ionian Basin. (a) From a continuous and expanded seismic sequence (multichannel seismic reflection profile MEM-07-104, shown in Figure 9b, in two-way travel time domain), we have obtained a depth-domain representation of the interpreted units using the post-Messinian interval velocity of 1780 m/s (Micallef et al., 2018). (b) Sedimentation rate of DSDP Site 374 in the Messina abyssal plain, showing a drastic increase upwards from the lower Pliocene to the Pleistocene. This sedimentation rate curve has been extrapolated proportionally to the sedimentary succession in (a), assuming that unit 1b is deposited instantaneously. In this way, the age of unit 1b is ~ 1.8 Ma, in the lower Pleistocene. (c) Summary stratigraphic scheme resulting from the merging of seismo-stratigraphic characteristics decribed in the text and age model derived in (a) and (b). Note that our nomenclature and that of DSDP Site 374 are different. MTD = Mass Transport Deposit.

Figure 3: (a) Sketch of the computational domain, boundary conditions and initial condition for the optimal streamflow (47.4 Sv) and pre-flood sea level (-1900 m). The corresponding flow depth is shown in panel (b). (c) Simulated water level and (d) flow depth at steady-state.

Figure 4: Multichannel seismic reflection profile MEM-07-102 showing units 3a and 3b and associated features of interest. Units 1 and 2, and horizons A-D, are also shown.

Figure 5: (a) Interpolated top surface of unit 3a (depth below present sea level; contour interval of 250 m). (b) Topographic profile A-B. (c) Topographic profile C-D.

Figure 6: (a) Multichannel seismic reflection profile MEM-07-203 showing unit 2 and associated features of interest. Units 1a, 1b and 1c, and horizons C-F, are also shown. (b) Zoomed section of part of figure 6a. (c) Multichannel seismic reflection profile CUMECS-3, showing units 1, 2 and associated features of interest. Locations in figure 1.

Figure 7: (a) Interpolated top surface of unit 2 (depth below present sea level; contour interval of 500 m). (b) Interpolated isopach map of unit 2 (contour interval of 115/130 m).

Figure 8: Map of units 1b, 1c and 2, and features of interest interpreted in seismic reflection profiles.

Figure 9: (a) Multichannel seismic reflection profile MEM-07-104 showing unit 1b and associated features of interest. Units 1a, 1c and 2, and horizons C-F, are also shown. (b) Zoomed section of part of figure 9a. Locations in figure 1.

Figure 10: (a) Multichannel seismic reflection profile CIR-04 showing units 1a and 1c and associated features of interest. Unit 1b and horizons D-F are also shown. (b) Multichannel

seismic reflection profile CA99-214 showing a chaotic sub-unit within unit 1a. Locations in figure 1.

Figure 11: Interpolated isopach map of unit 1c (contour interval of 30 m).

Figure 12: (a) Interpolated top surface of unit 1b (depth below present sea level; contour interval of 300 m). (b) Interpolated isopach map of unit 1b (contour interval of 115/130 m). (c) Zoomed bathymetric map of Noto Canyon (location in figure 12a).

Figure 13: (a) Simulated velocity magnitude for 47.4 Sv discharge and water levels between -1700 and -2400 m in the western Ionian Basin. Red line indicates the location of the inflow boundary condition. Location in figure 7a. RZ = recirculation zone. (b) Velocity magnitude of a theoretically smaller flood event with discharge of 20, 15, 10 and 5 Sv for an initial water level of -900 m. The area of unit 1b is denoted by a black line.

Figure 14: (a) Simulated water flow velocity and streamlines for -1900 m water level scenario and 47.4 Sv discharge in figure 13a, overlain by the isopach map of unit 2 (contour interval of 50 m). Red line indicates the location of the inflow boundary condition. RZ = recirculation zone. (b) Zoomed section of figure 14a showing the simulated Froude (Fr) number overlain by the isopach map of unit 2. Location in figure 14a.

Figure 15: Simulated water flow velocities for discharges of 47.4, 25, 10 and 2 Sv with -1900 m pre-flood water level, and associated estimates of the size of deposited sediment. Location in figure 7a.

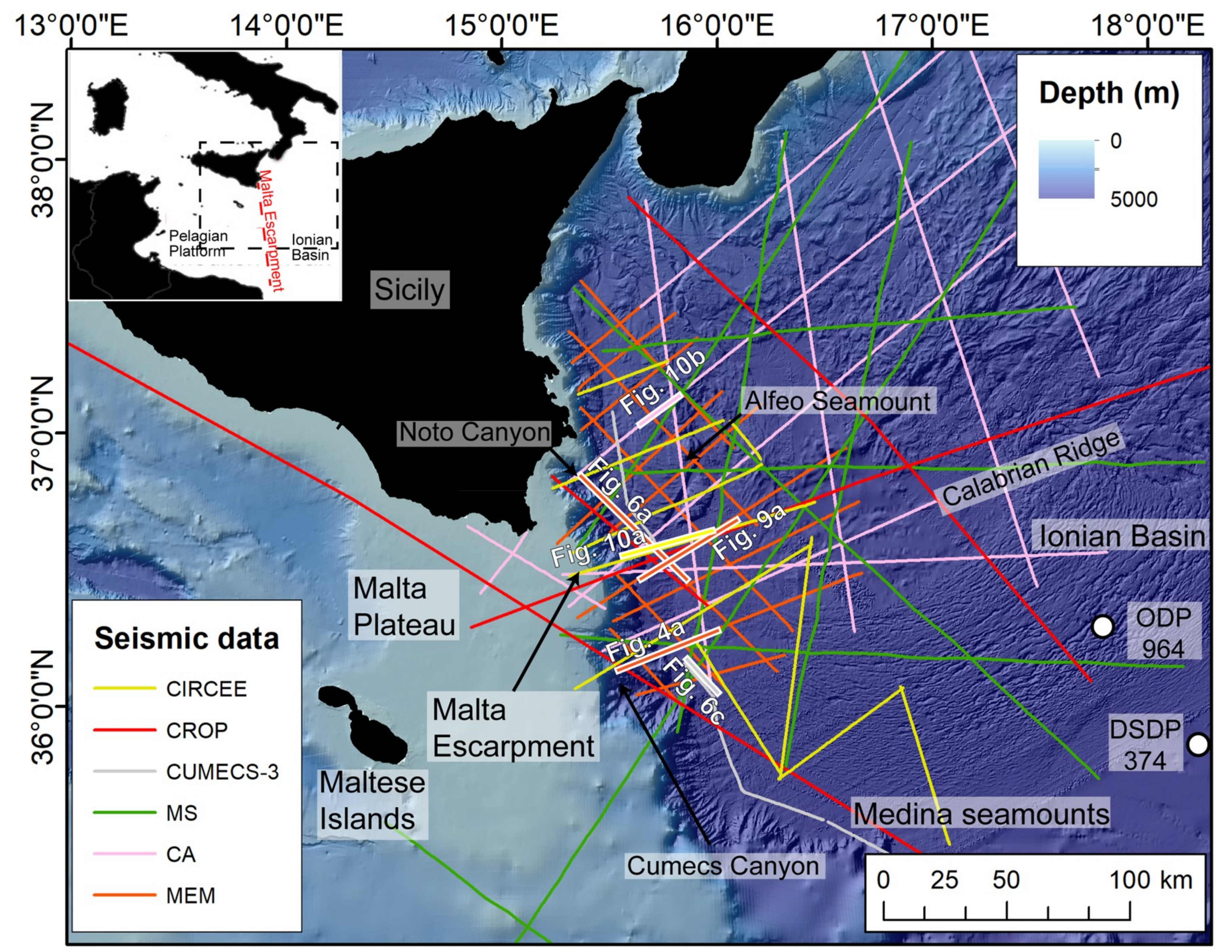

13°0'0"E
14°0'0"E
15°0'0"E
16°0'0"E
17°0'0"E
18°0'0"E
38°0'0"N
37°0'0"N
36°0'0"N
Pelagian Platform
Malta Escarpment
Ionian Basin
Sicily
Depth (m)
0
5000
Fig. 10b
Alfeo Seamount
Noto Canyon
Calabrian Ridge
Fig. 6a
Fig. 9a
Fig. 10a
Ionian Basin
Malta Plateau
ODP 964
Seismic data
Fig. 4a
CIRCEE
Fig. 6c
CROP
Malta Escarpment
DSDP 374
CUMECS-3
Maltese Islands
MS
Medina seamounts
CA
Cumecs Canyon
MEM
0 25 50 100 km

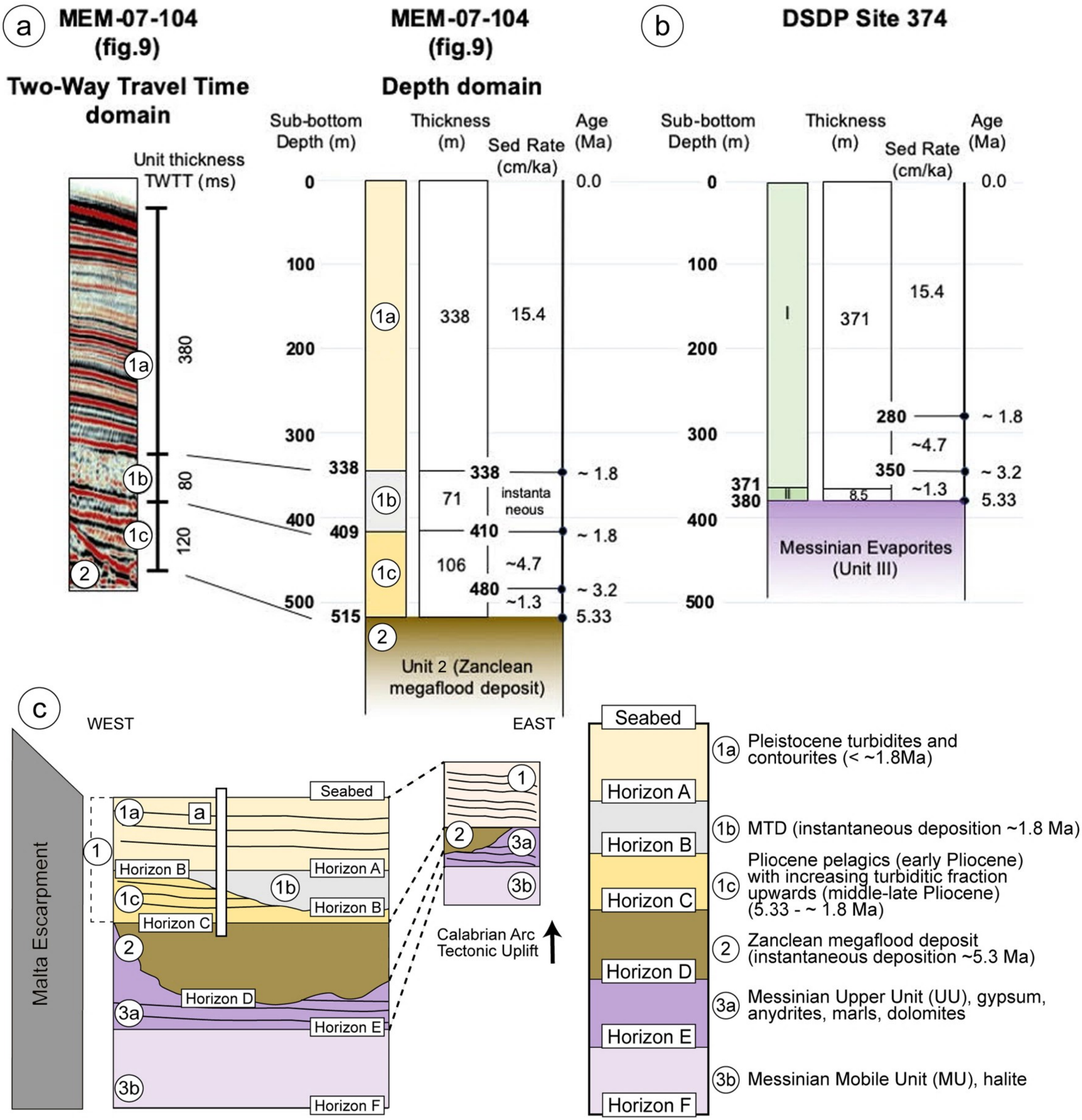

a
MEM-07-104 (fig.9)
Two-Way Travel Time domain
Unit thickness TWTT (ms)
380
80
120
1a
1b
1c
2
MEM-07-104 (fig.9)
Depth domain
Sub-bottom Depth (m)
Thickness (m)
Sed Rate (cm/ka)
Age (Ma)
0
100
200
300
338
400
409
500
515
338
71
106
410
480
15.4
instanta neous
~4.7
~1.3
0.0
~ 1.8
~ 1.8
~ 3.2
5.33
Unit 2 (Zanclean megaflood deposit)
b
DSDP Site 374
Sub-bottom Depth (m)
Thickness (m)
Sed Rate (cm/ka)
Age (Ma)
371
380
I
II
371
8.5
280
350
15.4
~4.7
~1.3
0.0
~ 1.8
~ 3.2
5.33
Messinian Evaporites (Unit III)
c
WEST
EAST
Malta Escarpment
Seabed
Horizon A
Horizon B
Horizon C
Horizon D
Horizon E
Horizon F
a
1
1a
1b
1c
2
3a
3b
Calabrian Arc Tectonic Uplift
Pleistocene turbidites and contourites (< ~1.8Ma)
MTD (instantaneous deposition ~1.8 Ma)
Pliocene pelagics (early Pliocene) with increasing turbiditic fraction upwards (middle-late Pliocene) (5.33 - ~ 1.8 Ma)
Zanclean megaflood deposit (instantaneous deposition ~5.3 Ma)
Messinian Upper Unit (UU), gypsum, anydrites, marls, dolomites
Messinian Mobile Unit (MU), halite

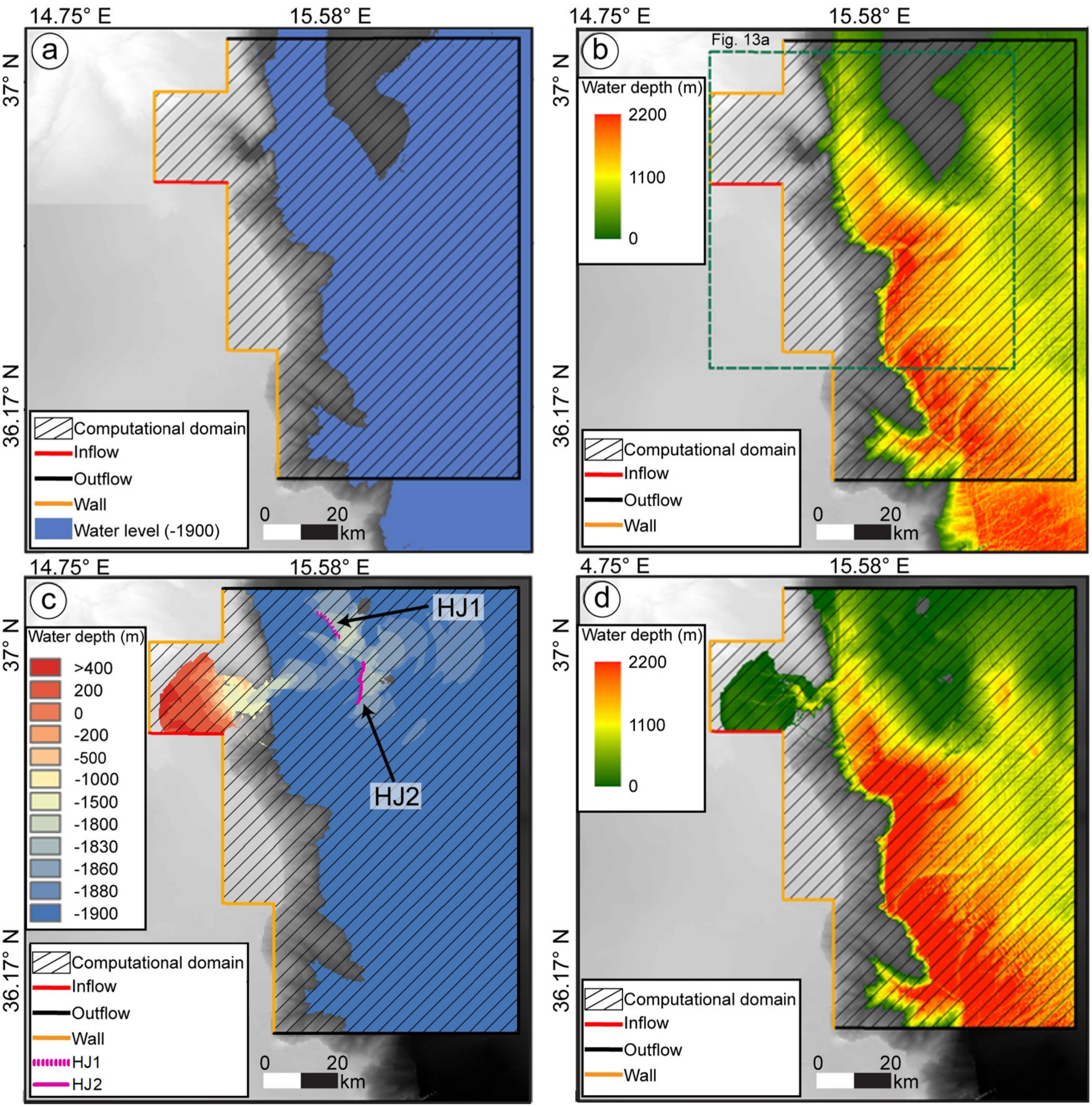

14.75° E
15.58° E
37° N
36.17° N
a
Computational domain
Inflow
Outflow
Wall
Water level (-1900)
0
20
km
b
Fig. 13a
Water depth (m)
2200
1100
0
c
HJ1
HJ2
>400
200
-200
-500
-1000
-1500
-1800
-1830
-1860
-1880
-1900
d
4.75° E

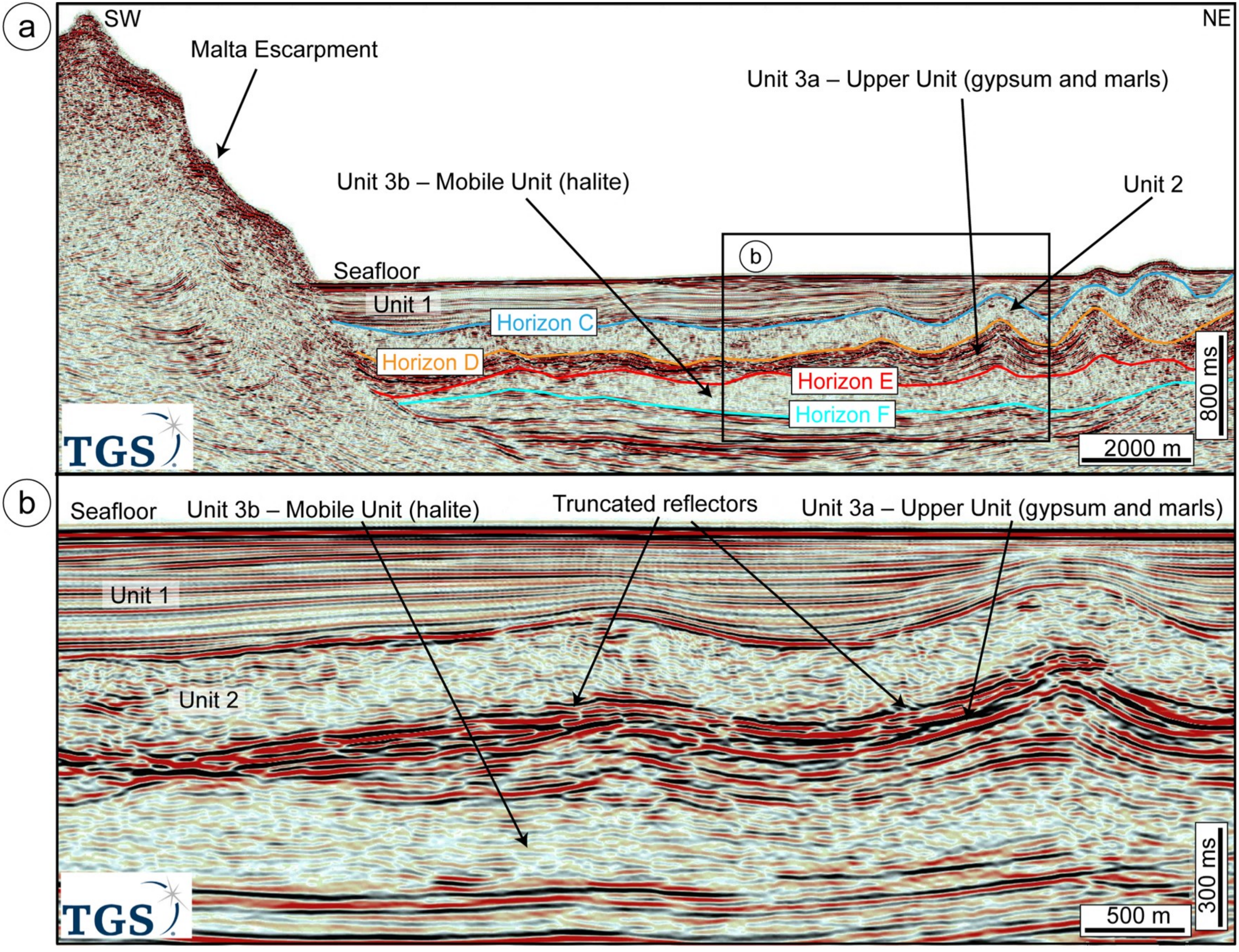
a
SW
NE
Malta Escarpment
Unit 3a – Upper Unit (gypsum and marls)
Unit 3b – Mobile Unit (halite)
Unit 2
b
Seafloor
Unit 1
Horizon C
Horizon D
Horizon E
Horizon F
800 ms
2000 m
TGS
b
Seafloor
Unit 3b – Mobile Unit (halite)
Truncated reflectors
Unit 3a – Upper Unit (gypsum and marls)
Unit 1
Unit 2
300 ms
500 m
TGS

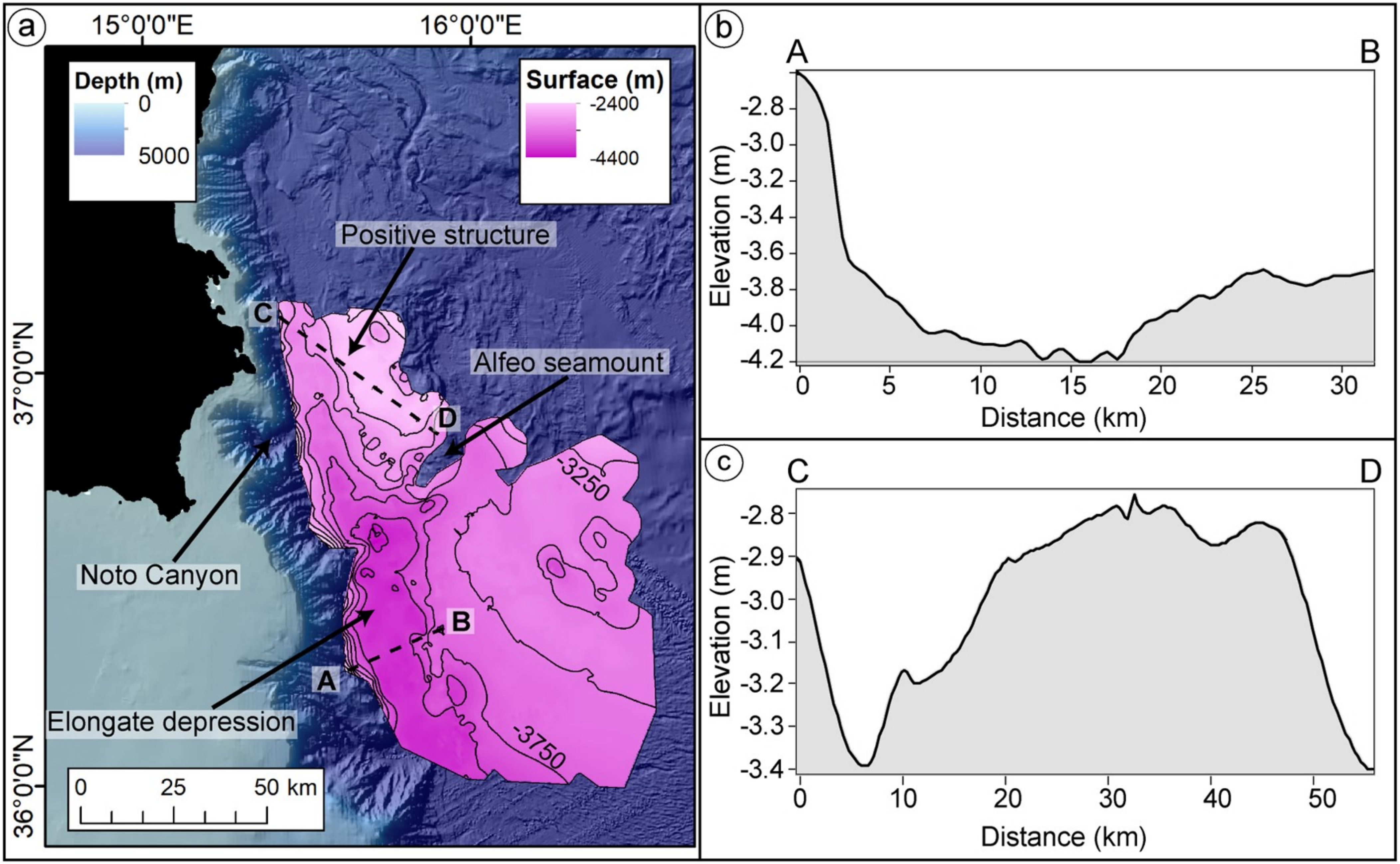
a
15°0'0"E
16°0'0"E
37°0'0"N
36°0'0"N
Depth (m)
0
5000
Surface (m)
-2400
-4400
Positive structure
Alfeo seamount
Noto Canyon
Elongate depression
C
D
A
B
-3250
-3750
0
25
50 km
b
A
B
Elevation (m)
-2.8
-3.0
-3.2
-3.4
-3.6
-3.8
-4.0
-4.2
0
5
10
15
20
25
30
Distance (km)
c
C
D
Elevation (m)
-2.8
-2.9
-3.0
-3.1
-3.2
-3.3
-3.4
0
10
20
30
40
50
Distance (km)

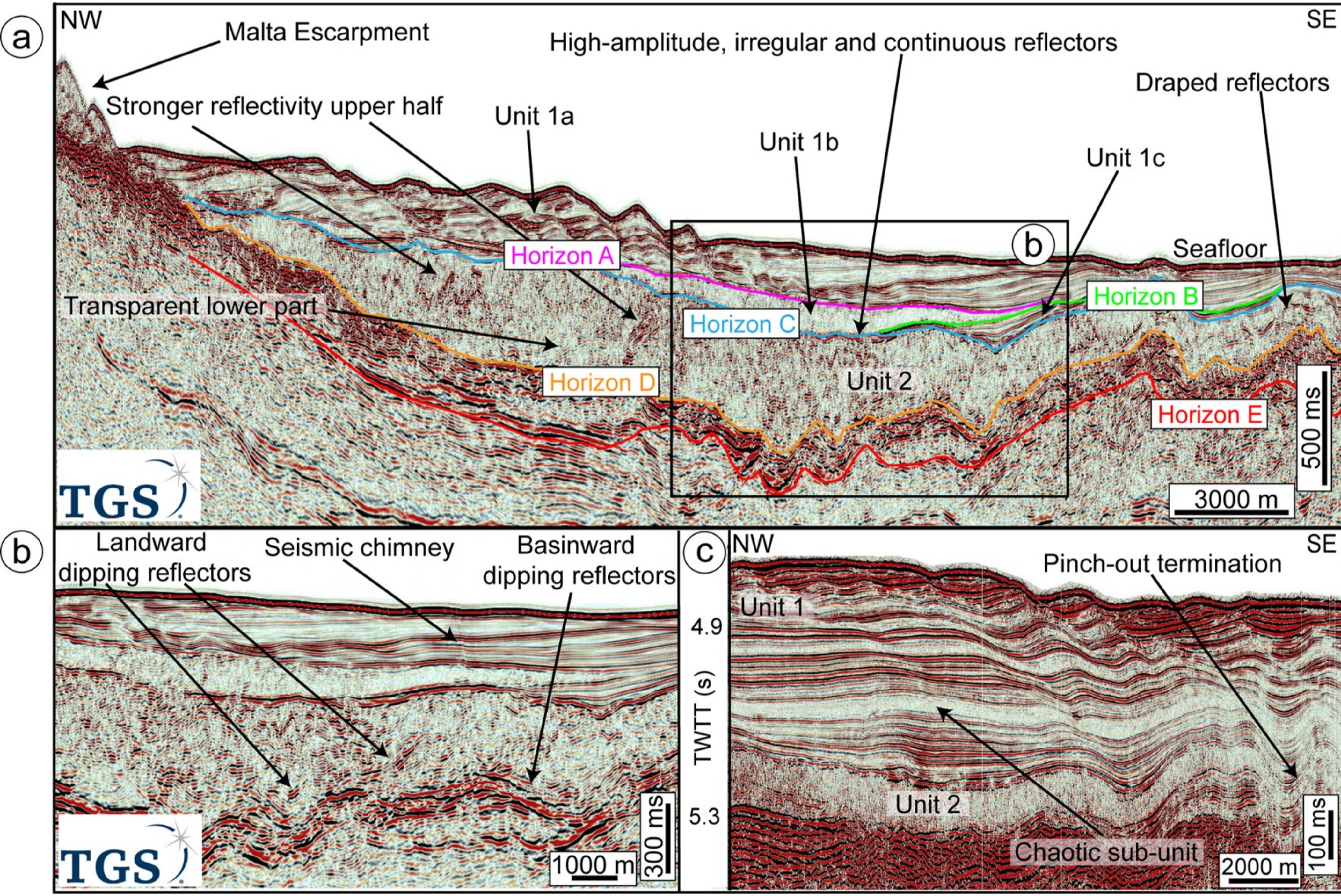

a
NW
SE
Malta Escarpment
High-amplitude, irregular and continuous reflectors
Draped reflectors
Stronger reflectivity upper half
Unit 1a
Unit 1b
Unit 1c
b
Seafloor
Horizon A
Horizon B
Horizon C
Transparent lower part
Unit 2
Horizon D
Horizon E
500 ms
3000 m
TGS
b
Landward dipping reflectors
Seismic chimney
Basinward dipping reflectors
1000 m
300 ms
TGS
c
NW
SE
Pinch-out termination
Unit 1
4.9
TWTT (s)
5.3
Unit 2
Chaotic sub-unit
2000 m
100 ms

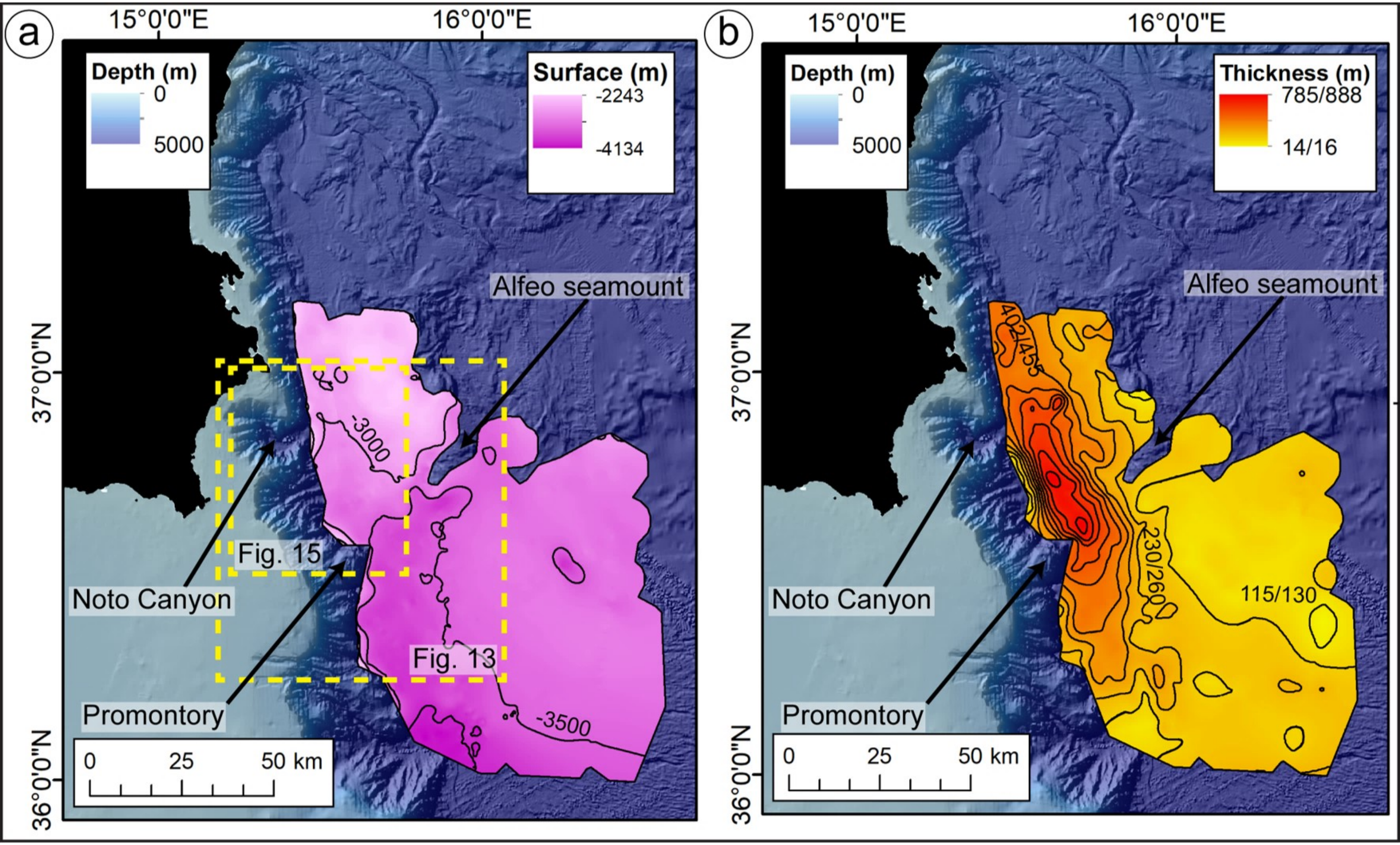

a
15°0'0"E
16°0'0"E
37°0'0"N
36°0'0"N
Depth (m)
0
5000
Surface (m)
-2243
-4134
Alfeo seamount
-3000
-3500
Fig. 15
Fig. 13
Noto Canyon
Promontory
0
25
50 km
b
15°0'0"E
16°0'0"E
37°0'0"N
36°0'0"N
Depth (m)
0
5000
Thickness (m)
785/888
14/16
Alfeo seamount
402/455
230/260
115/130
Noto Canyon
Promontory
0
25
50 km

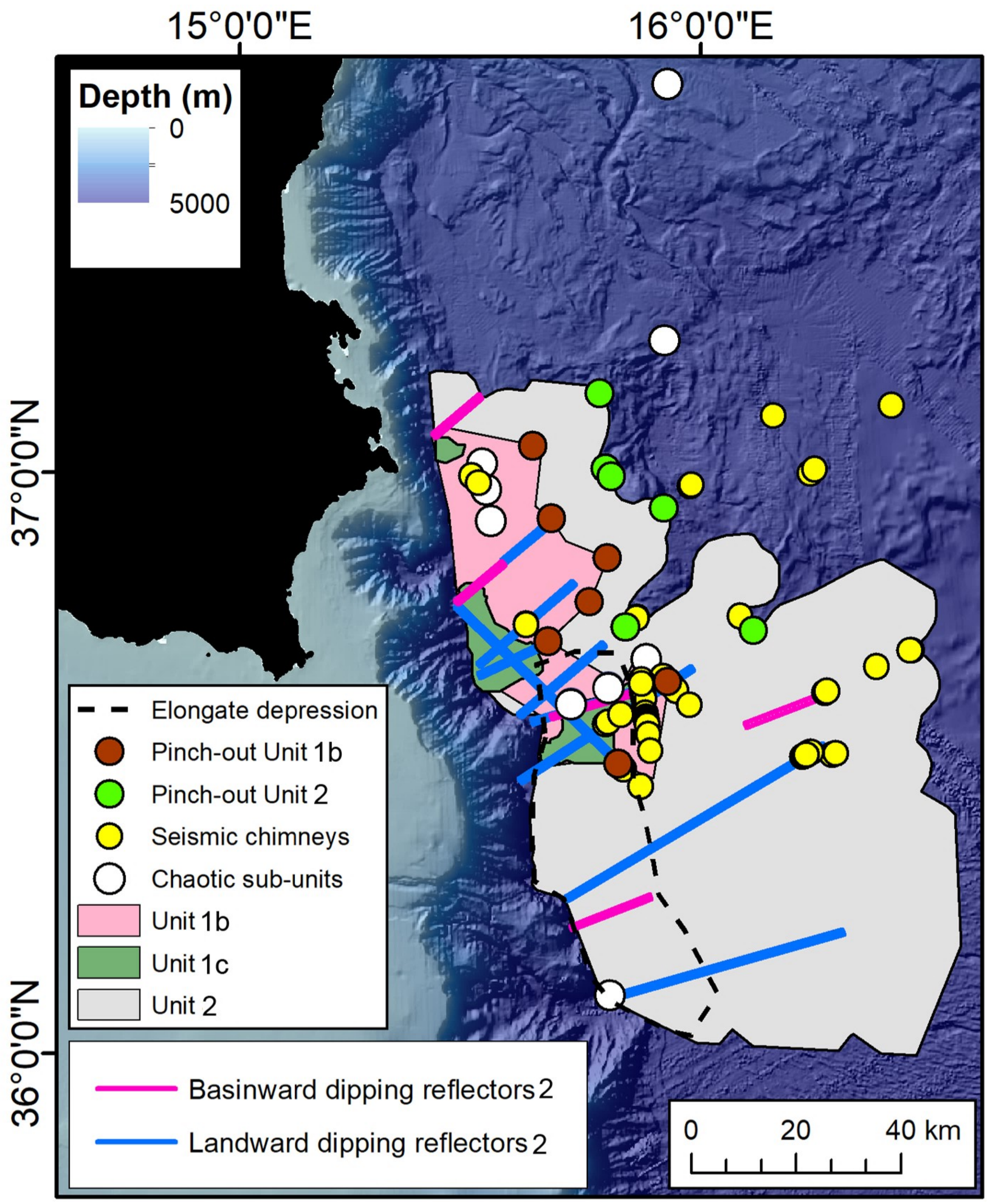
15°0'0"E
16°0'0"E
37°0'0"N
36°0'0"N
Depth (m)
0
5000
Elongate depression
Pinch-out Unit 1b
Pinch-out Unit 2
Seismic chimneys
Chaotic sub-units
Unit 1b
Unit 1c
Unit 2
Basinward dipping reflectors 2
Landward dipping reflectors 2
0
20
40 km

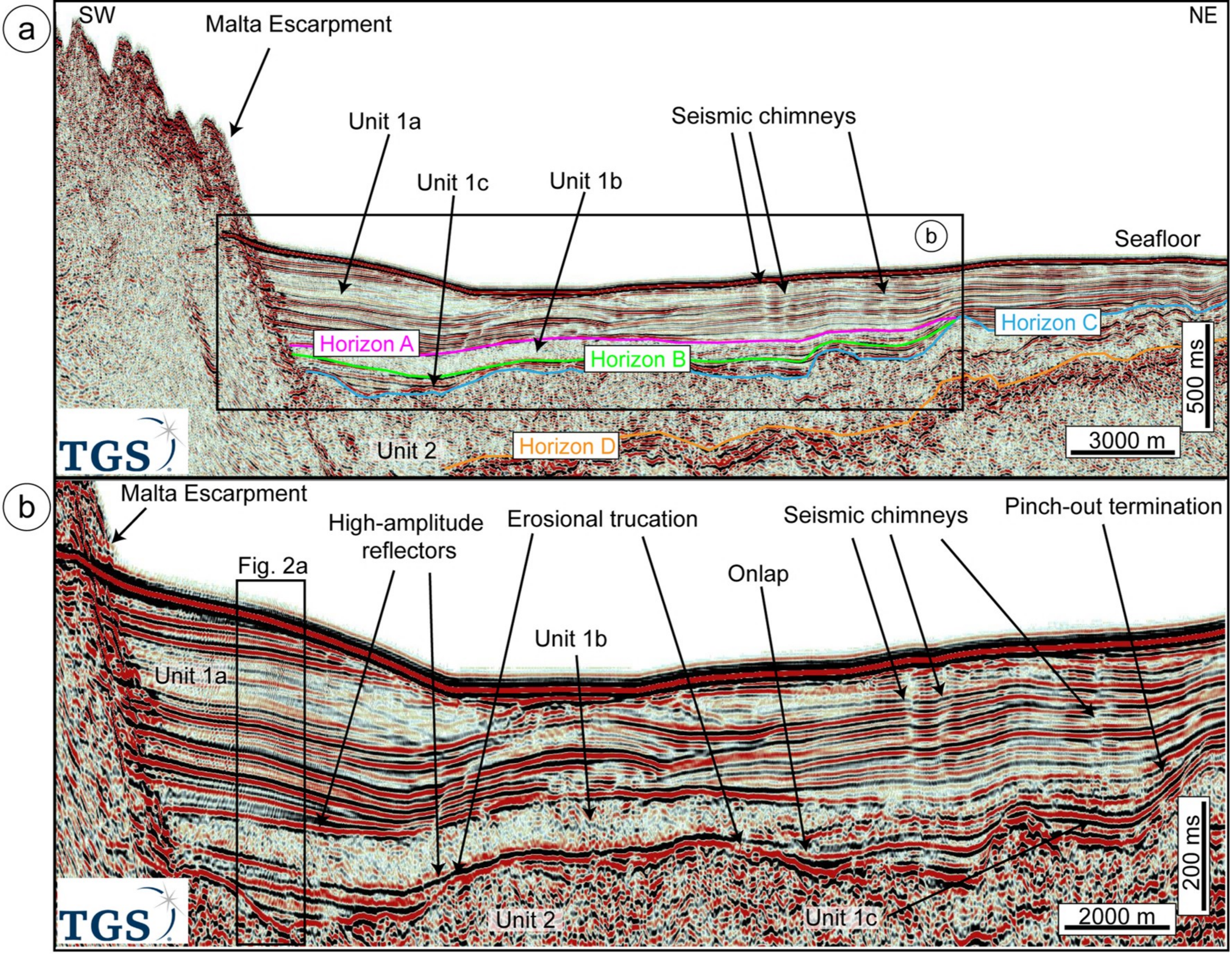
a
SW
NE
Malta Escarpment
Unit 1a
Seismic chimneys
Unit 1c
Unit 1b
b
Seafloor
Horizon A
Horizon B
Horizon C
500 ms
Unit 2
Horizon D
3000 m
TGS
b
Malta Escarpment
High-amplitude reflectors
Erosional trucation
Seismic chimneys
Pinch-out termination
Fig. 2a
Onlap
Unit 1b
Unit 1a
200 ms
Unit 2
Unit 1c
2000 m
TGS

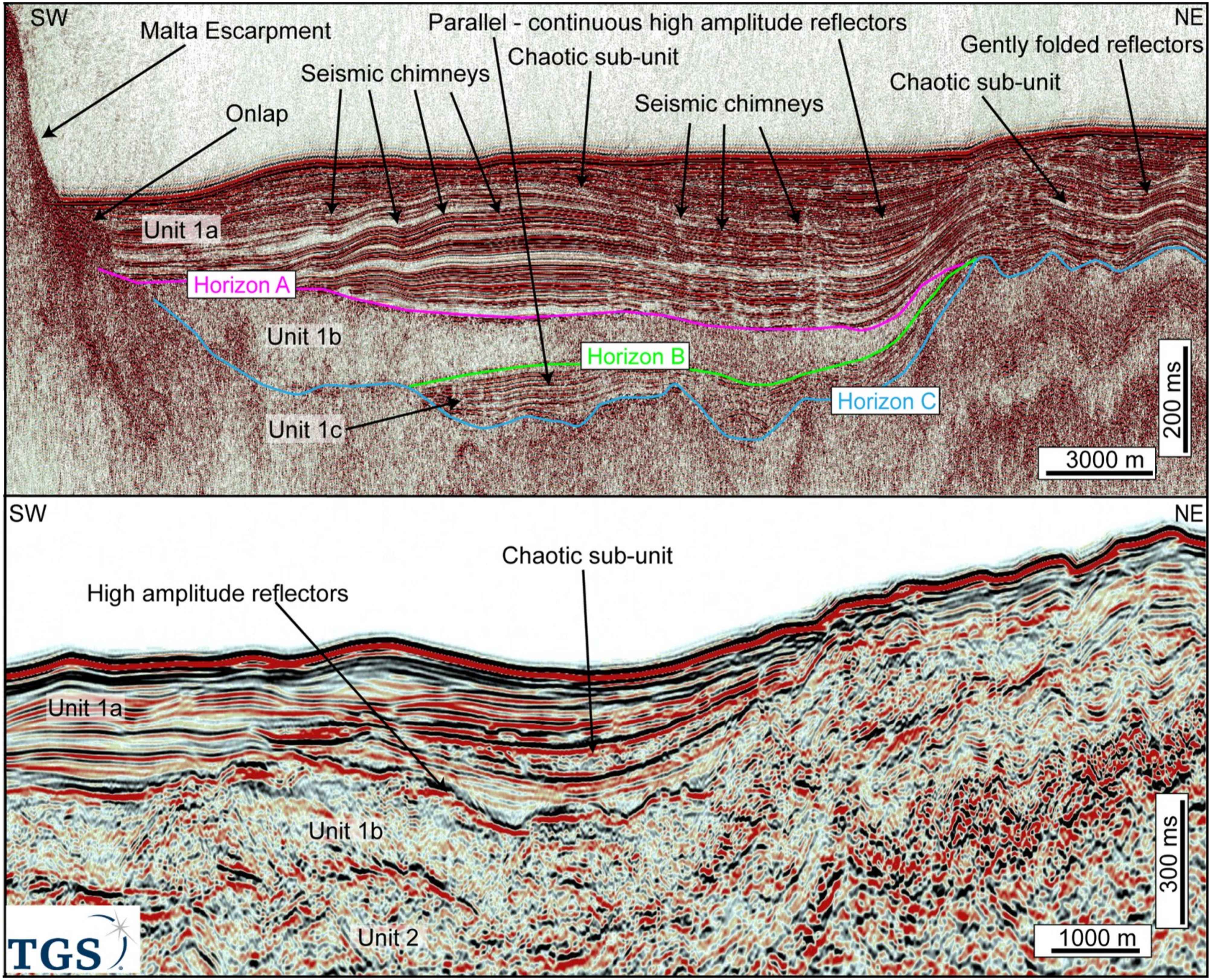
a
SW
NE
Malta Escarpment
Parallel - continuous high amplitude reflectors
Gently folded reflectors
Seismic chimneys
Chaotic sub-unit
Chaotic sub-unit
Seismic chimneys
Onlap
Unit 1a
Horizon A
Unit 1b
Horizon B
Horizon C
Unit 1c
200 ms
3000 m
b
SW
NE
Chaotic sub-unit
High amplitude reflectors
Unit 1a
Unit 1b
Unit 2
300 ms
1000 m
TGS

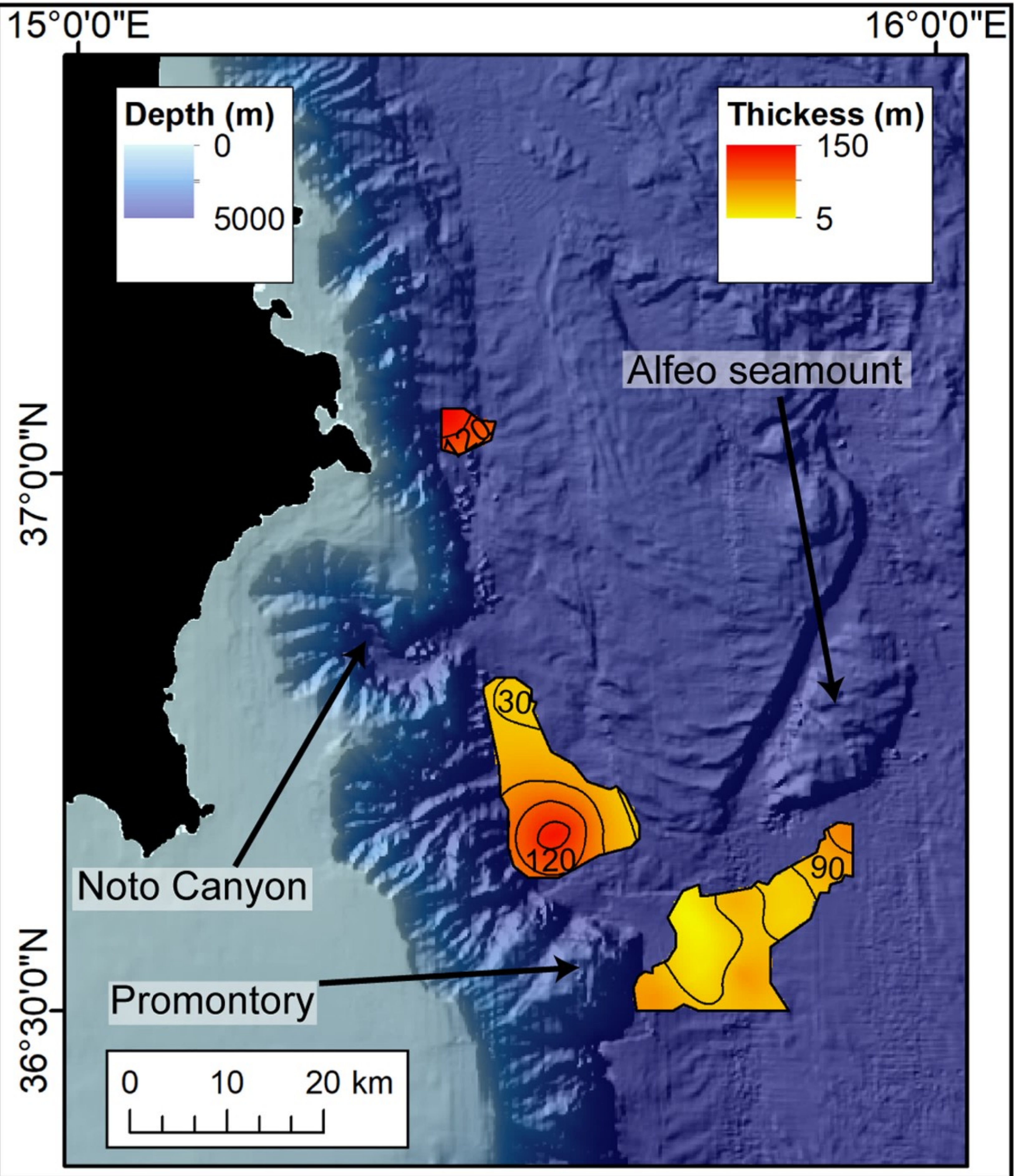

15°0'0"E
16°0'0"E
37°0'0"N
36°30'0"N
Depth (m)
0
5000
Thickess (m)
150
5
Alfeo seamount
Noto Canyon
Promontory
120
30
120
90
0
10
20 km

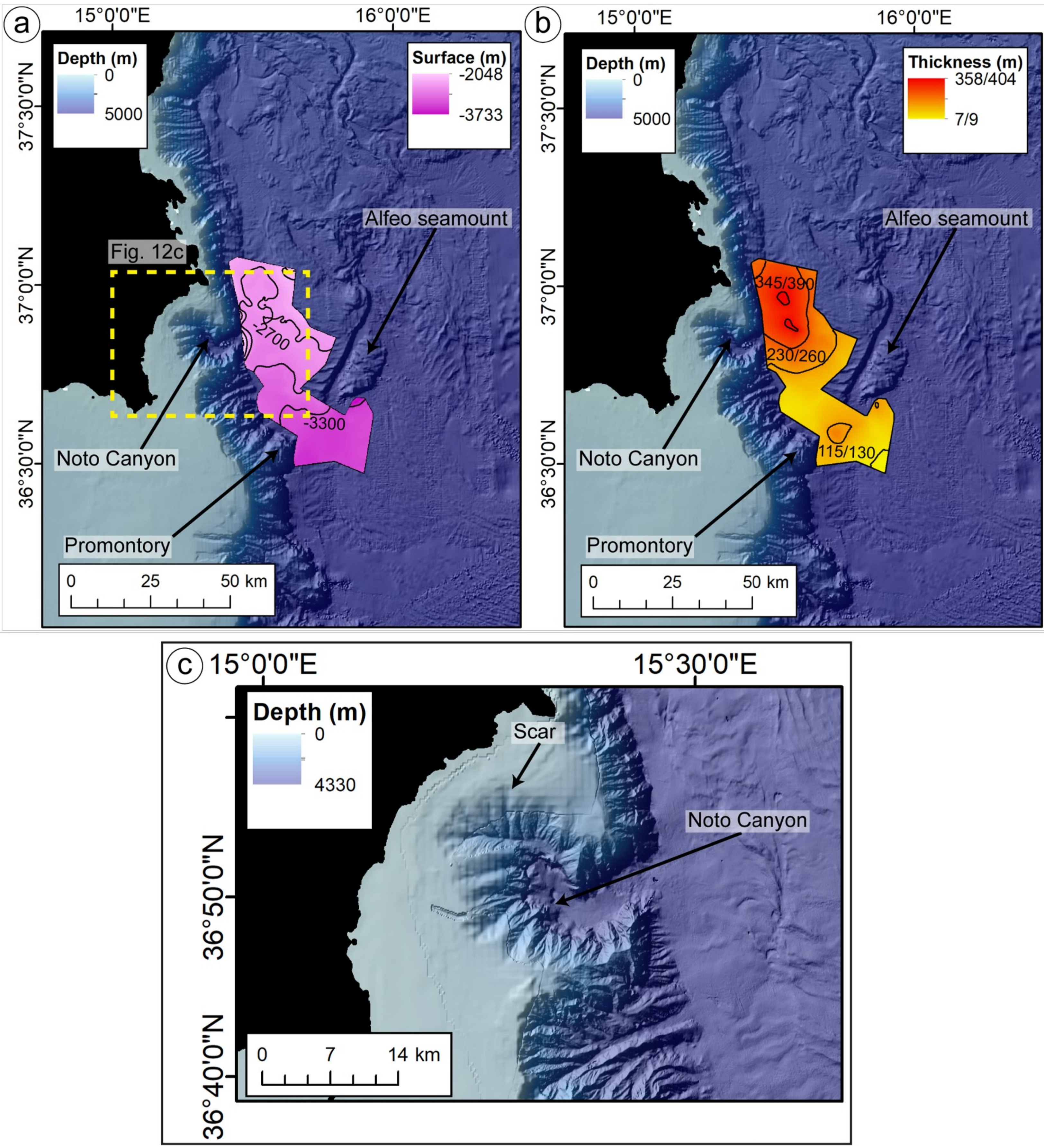
a
15°0'0"E
16°0'0"E
37°30'0"N
37°0'0"N
36°30'0"N
Depth (m)
0
5000
Surface (m)
-2048
-3733
Alfeo seamount
Fig. 12c
-2700
-3300
Noto Canyon
Promontory
0
25
50 km
b
15°0'0"E
16°0'0"E
37°30'0"N
37°0'0"N
36°30'0"N
Depth (m)
0
5000
Thickness (m)
358/404
7/9
Alfeo seamount
345/390
230/260
115/130
Noto Canyon
Promontory
0
25
50 km
c
15°0'0"E
15°30'0"E
36°50'0"N
36°40'0"N
Depth (m)
0
4330
Scar
Noto Canyon
0
7
14 km

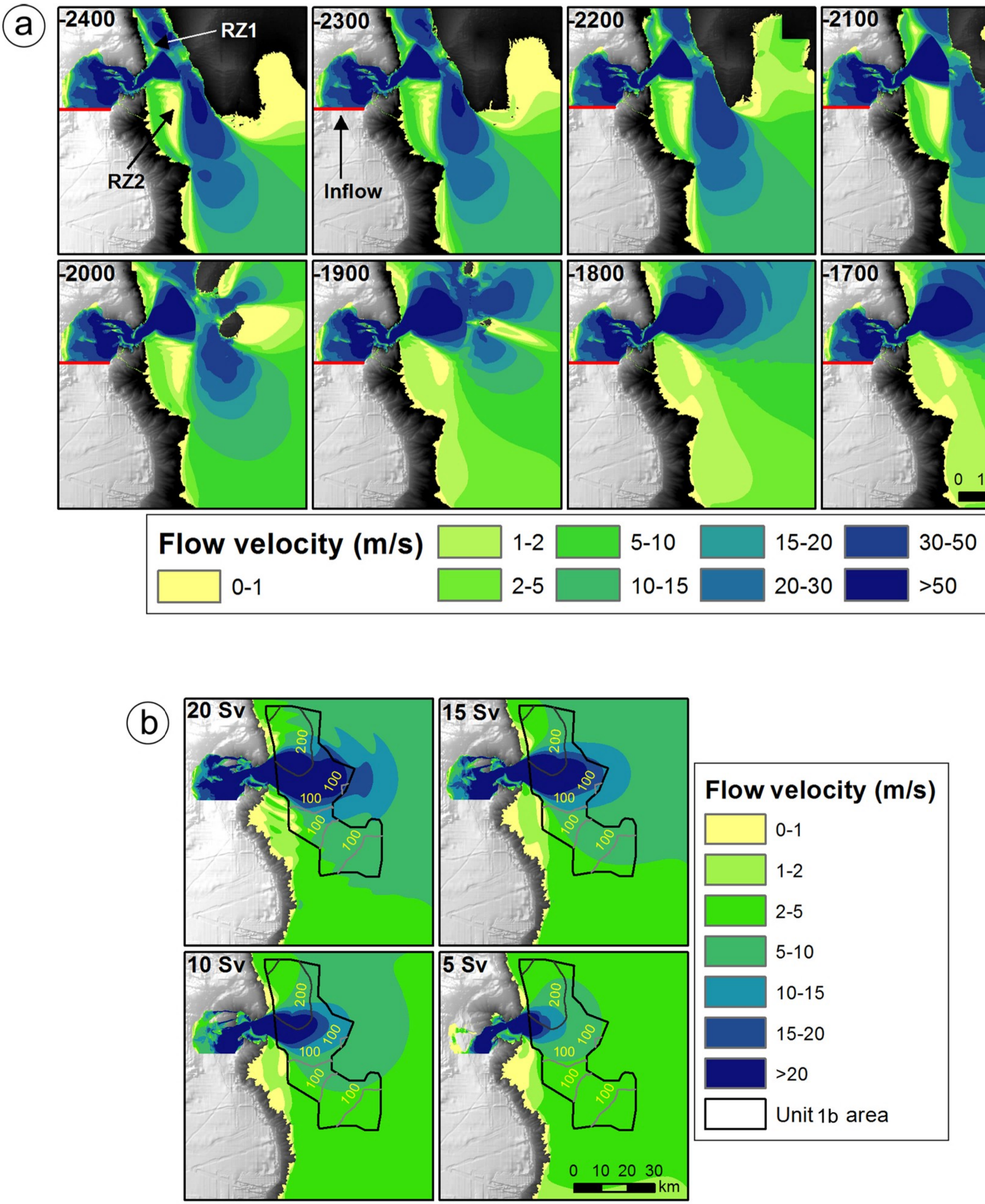

a
-2400
RZ1
RZ2
-2300
Inflow
-2200
-2100
-2000
-1900
-1800
-1700
0 10 20 30
km
Flow velocity (m/s)
0-1
1-2
2-5
5-10
10-15
15-20
20-30
30-50
>50
b
20 Sv
15 Sv
10 Sv
5 Sv
200
100
0 10 20 30
km
Flow velocity (m/s)
0-1
1-2
2-5
5-10
10-15
15-20
>20
Unit 1b area

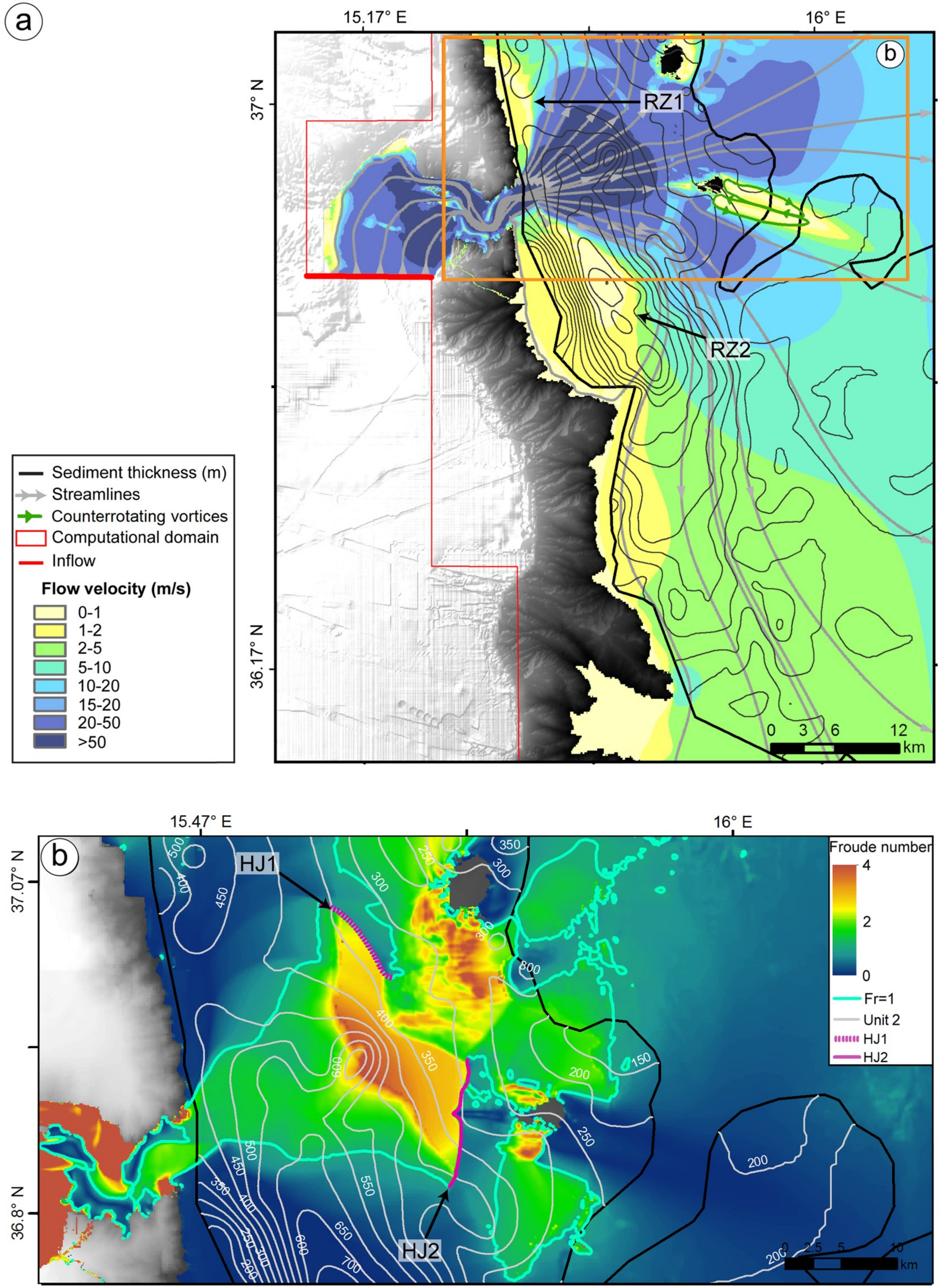

a
15.17° E
16° E
37° N
36.17° N
b
RZ1
RZ2
0 3 6 12 km
Sediment thickness (m)
Streamlines
Counterrotating vortices
Computational domain
Inflow
Flow velocity (m/s)
0-1
1-2
2-5
5-10
10-20
15-20
20-50
>50
15.47° E
16° E
37.07° N
36.8° N
HJ1
HJ2
Froude number
4
2
0
Fr=1
Unit 2
HJ1
HJ2
0 2.5 5 10 km

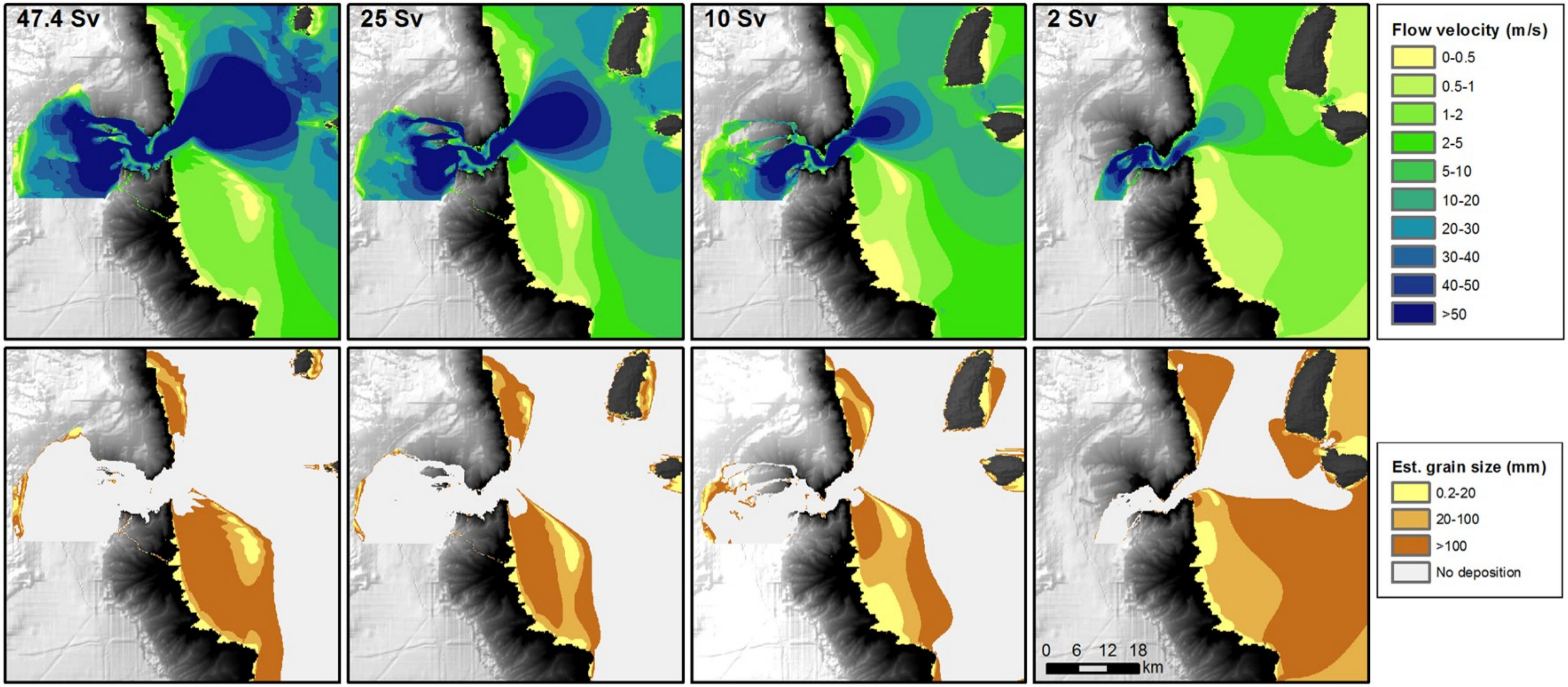
47.4 Sv
25 Sv
10 Sv
2 Sv
Flow velocity (m/s)
0-0.5
0.5-1
1-2
2-5
5-10
10-20
20-30
30-40
40-50
>50
Est. grain size (mm)
0.2-20
20-100
>100
No deposition
0 6 12 18
km